DESIGN AND MODELING OF TUNABLE MICROFLUIDIC DEVICES FOR LABEL-FREE SEPARATION OF CIRCULATING TUMOR CELLS

By

MOHAMMED RAIHAN UDDIN

A thesis submitted in partial fulfillment of
the requirements for the degree of

MASTER OF SCIENCE IN MECHANICAL ENGINEERING

WASHINGTON STATE UNIVERSITY
School of Engineering and Computer Science, Vancouver

MAY 2023

To the Faculty of Washington State University:

The members of the Committee appointed to examine the thesis of MOHAMMED RAIHAN UDDIN find it satisfactory and recommend that it be accepted.

_____

Xiaolin Chen, Ph.D., Chair

_____

Hua Tan, Ph.D.

_____

Jong-Hoon Kim, Ph.D.

ACKNOWLEDGMENT

First, I want to express my earnest gratitude to my advisor, Dr. Xiaolin Chen, for her continuous support and motivation throughout my graduate study and research. I appreciate her spirit of adventure to explore new ideas without being afraid of failure. Without her guidance, critical reviews, and persistent help as a great mentor, it would not be possible to improve my research capability and writing.

My sincere thanks to Dr. Jong-Hoon Kim for being my committee member and for his course on microfabrication technology, in which I gained valuable practical experiences related to this field. I would like to thank Dr. Hua Tan for being my committee member and for his valuable courses on Computational Fluid Dynamics and Heat Transfer, which have been an asset and valuable tool for my graduate research.

I wish to express my gratitude to my friends, classmates, and well-wishers who have given me a wonderful time, support, and suggestions.

Finally, I want to express my heartfelt thanks to my mom and every member of my family for their love and support and tireless efforts to make my journey a memorable one.

DESIGN AND MODELING OF TUNABLE MICROFLUIDIC DEVICES FOR LABEL-FREE SEPARATION OF CIRCULATING TUMOR CELLS

Abstract

by Mohammed Raihan Uddin, M.S.
Washington State University
May 2023

Chair: Xiaolin Chen

Reliable separation and detection of circulating tumor cells from blood cells are crucial for early cancer diagnosis and prognosis. Many conventional microfluidic platforms take advantage of the size difference between particles for their separation, which renders them impractical for sorting overlapping-sized cells. To address this concern, a hybrid inertial-dielectrophoretic microfluidic chip is proposed in this work for continuous and single-stage separation of lung cancer cell line A549 cells from white blood cells of overlapping size. The working mechanism of the proposed spiral microchannel embedded with planar interdigitated electrodes is validated against the experimental results in the existing literature. A numerical investigation is carried out over a range of flow conditions and electric field intensity to determine the separation efficiency and migration characteristics of the cell mixture. The results demonstrate the unique capability of the proposed microchannel to achieve high-throughput separation of cells (~0.7mL/min) at low applied voltages (~10V) in both vertical and lateral directions. A significant lateral separation distance between the CTCs and the WBCs has been achieved, which allows for high-resolution and effective separation of cells. The separation resolution can be controlled by adjusting the

strength of the applied electric field. Furthermore, the results demonstrate that the lateral separation distance is maximum at a voltage termed as the critical voltage, which increases with the increase in the flow rate. Moreover, several electrode configurations have been studied, and it was found that better separation can be achieved with a higher number of electrodes also, positioning the electrodes towards the beginning of the channel makes them more effective for cell separation. Additionally, the robustness of the system was studied by using a mixture of WBCs containing four main subtypes having different sizes and dielectric properties. The electrode-embedded spiral microchannel was successful in separating the CTCs from the mixture of WBCs. The proposed microchannel and the developed technique can provide valuable insight into the development of a tunable and robust point-of-care device for effective and high-throughput separation of cancer cells from the WBCs.

TABLE OF CONTENTS

LIST OF TABLES

Page

LIST OF FIGURES

Page

Dedication

To my mom, who means the world to me.

.

CHAPTER 1: INTRODUCTION

1.1 Overview of Circulating Tumor Cells (CTCs)

The ability to sort, separate and purify cells in biological samples is an indispensable step in the fundamental research, diagnosis, and treatment of various life-threatening diseases like cancer [1]. Cancer is the second leading cause of death in the United State and each year more than 1.6 million people are diagnosed with it [2]. Biopsy for the separation and detection of cancer cells in the tissues causes patient discomfort including chronic pain, excessive internal bleeding, infection at the site, and puncture damage to nearby tissue or organs. In contrast, Circulating Tumor Cells (CTCs), a type of cancer cells shed into the bloodstream from either primary or metastatic tumors, can preserve the heterogeneity and properties of the tumor which allows them to be a vital clinical biomarker for dynamic monitoring of cancer. CTCs can be separated in non-invasive blood-based assays, i.e., liquid biopsy, to help discover the disease mechanism and develop drug and targeted therapies as liquid biopsies can be carried out at desired frequencies. The analysis of CTCs is an outstanding tool to provide critical insights into the diagnosis and prognosis of cancer and the efficacy of its treatment [3]. Despite the importance of CTCs in cancer management, the progress of CTCs research has been hindered by several factors including their extreme rarity (around 1 CTCs per 10^7 leukocytes) in the periphery of the blood and their significant size overlaps with the normal blood cells [4]. These characteristics make the separation and purification of CTCs from blood extremely difficult and subsequently challenging to formulate an effective cancer remedy.

1.2 Circulating tumor cells separation methods

Several CTC separation techniques have been developed over the years which exploit the difference in the biological or physical properties of cells. A biological marker is used in the FDA-approved method, CellSearch which is an immuno-affinity-based technique that uses a type of surface antigen called Epithelial Cell Adhesion Molecule (EpCAM) [5]. The captured cells can be positively identified using techniques such as fluorescence-activated cell sorting (FACS) or Magnetic activated cell sorting (MACS). These methods can provide an automated, robust, and highly accurate platform for cell sorting based on multiple morphological characteristics of the cells. Despite the advantages, these cell sorting platforms have some major hurdles to overcome including their high processing time, bulky instruments, high unit and sample processing cost as well as expertise needed to operate the complex machinery [6]. Another important challenge associated with using the biological marker is that some of the metastatic tumor cells undergo epithelial to mesenchymal transition (EMT), which results in loss of expression for the epithelial markers such as EpCAM. The loss of epithelial markers may result in false-negative findings [7].

The physical properties of the cells have been exploited in conventional cell separation techniques such as flow cytometry and density gradient centrifugation. These methods are reliable, inexpensive and label-free but they often suffer from low separation efficiency, long processing time and the loss of large cells [8]. To address these challenges, research is being carried out on the development of label-free microfluidic devices for effective CTC isolation. The label-free microfluidic chip provides numerous advantages compared to other traditional methods of cell separation including high throughput separation, parallelization of the processes, reduced size of the equipment and reduced complexity of the separation mechanism. In addition, microfluidic

separation can provide better resolution with lower sample volume and real-time tunability of the separation parameters [6], [9].

Primarily, label-free microfluidic separation devices can be divided into two major categories, namely, active, and passive devices [10], [11]. Active devices are reliant on the external field to achieve separation. They include, magnetophoresis [12], acoustophoresis [13], electrophoresis [14] and dielectrophoresis (DEP) [14]. Active devices such as DEP are often found to provide better tunability at the cost of lower throughput. Conventional DEP processing techniques are batch process which allows only a certain amount of sample volume to enter the chamber and undergo separation. Any high-throughput separation that are achieved in the batch processing devices is by highly paralleling the process [16]. However, the parallel configuration increases the complexity of the device and adds to the difficulty in handling and processing the sample. Additionally, in such devices, formation of "pearl-chain" due to induced dipole-dipole interaction between cells in the absence of any drag force causes clogging effect which may further reduce the throughput that can be achieved [17]. On the other hand, passive devices use the inherent properties of the particles, channel and underlying flow physics for separation. Passive separation techniques primarily include microfiltration [18], inertial microfluidics [19], deterministic lateral displacement (DLD) [20] and pinched flow fractionation [21]. Passive separation devices do not rely on an external field, and the separation can be continuous and high-throughput [22], [23]. However, tunability of the passive devices is a major hurdle as the fixed channel geometry restricts the types of samples that can be effectively analyzed by the device. To overcome the challenges of individual active and passive methods, hybrid devices have been developed that can benefit from both methods to achieve label-free, high throughput separation with excellent efficiency at the same time.

Recently, hybrid separation techniques utilizing the dielectric properties of the particles have garnered great attention as they have demonstrated effective separation results. The combination of DEP with other active techniques such as optic, magnetic and acoustic has been studied by several groups. In addition to active methods, DEP has also been combined with many passive platforms such as hydrophoresis [24] and multi-orifice flow fractionation [25]. To achieve continuous separation of particles, Beech et. al. [24] have developed a high-resolution, tunable particle separation device combining Dielectrophoresis and DLD. Additionally, continuous separation of MDA-231 breast cancer cells from white blood cells based on their size and dielectric properties has been achieved in a DLD device using insulator-based DEP at a high cross-over frequency of the particles in previous studies[26], [27]. DEP force has also been previously integrated with inertial devices to form hybrid devices. By exploiting the difference in the magnitude of the DEP force based on the size of the particles, the work of Church et. al. [28] and Zhu et. al. [29]aims to separate different sized particles at an arbitrarily low frequency (~1kHz) and a high voltage (~1000V). In these works, continuous separation is achieved by the differential cross-stream motion of particles, induced by the nonuniform electric field inherent in a curved channel. Due to having a larger diameter, the larger particles experience a higher negative DEP force, and are pushed more outwards across the channel whereas the smaller particles focus near the center of the channel. This ultimately results in two separate streams of particles. Similar to the previous works, Zhang et. al. [30] relies on the fact that the larger particles will experience higher negative DEP force and the critical voltage for the vertical separation of different sized particles in a binary particle mixture has been presented.

Recent studies suggest that CTCs may have a significant size overlap with WBCs. Marrinucci et. al. [31] have discovered CTCs in the body of colorectal cancer patients to be similar

in size or smaller than the WBCs. Jin et. al. [32] have also reported that the size of CTCs found in the body of prostate cancer patients has size overlaps with leukocytes. Lung carcinoma epithelial cells, A549, have significant size overlaps with WBCs. Owing to these facts, a high level of WBCs contamination may be observed in many of the previously mentioned devices. To overcome this challenge, Khan and Chen and Islam et. al. [33], [34] developed hybrid platforms utilizing the dielectric property difference between CTCs and WBCs to achieve breast cancer cell separation in serpentine and zig-zag microchannels. However, the proposed channels can separate cells with a low separation distance which can cause difficulties in controlling the precision of cell separation, moreover, the separation was demonstrated by using dielectrophoretic forces at a high AC electric field voltage in the study which may result in electroporation or electrodestruction of the cells [35].

1.3 Research Motivation

The ability to effectively separate CTCs from a mixtrure of WBCs at a fast rate without damaging them is crucial in biomedical applications. In this study, to achieve high throughput, separation of CTC from the blood cells, we propose a hybrid separation mechanism using embedded DEP electrodes in a spiral microchannel. Spiral microchannels are simple yet provide an effective medium for high throughput separation of particles and in the proposed technique, the planar interdigitated electrodes are embedded on the same microchannel for simplicity rather than creating a two-stage separation device. The technique utilizes the DEP force for efficient separation based on the different dielectric properties of the suspended cells, and leverages from the inertial channel to come up with high-speed continuous separation at the same time. The hybrid design allows for elimination of the size-dependent separation inherent in the conventional inertial microfluidics and surpasses the conventional DEP devices by providing continuous high

throughput separation without the high complexity of parallel microfluidic channel layouts. To the best of our knowledge, no prior work has been carried out for the overlapping size separation of CTCs in a spiral inertial microfluidic platform. In this paper, separation of CTCs from WBCs, irrespective of their sizes is achieved with a large separation distance at a small voltage using the proposed hybrid inertial-dielectrophoretic spiral microchannel. Both the vertical and the lateral migration of cells are utilized for separation through the combined action of the dean flow, the lift and the DEP forces. In this work, the effectiveness of the system to separate CTCs from a mixture containing various subtypes of WBCs is also demonstrated. Moreover, the effects of the Reynolds number and the operating voltage and the configuration of electrodes on the migration characteristics and the separation distance of the cells are also examined to determine the optimum operating conditions for cell separation.

1.4 Thesis Outline

The first chapter of this book provides an overview of circulating tumor cells (CTCs) and its importance in both the importance of cell separation both in therapeutics and diagnostic application for cancer treatment. Next, the existing methods to separate CTCs from other blood cells and their limitations is discussed. The motivation for undertaking subsequent research is also briefly discussed at the end of this chapter.The next chapter provides an in-depth discussion of the related theory behind the separation of CTCs from blood cells using hybrid inertial microfluidics. It covers the fundamental principle of microfluidic devices and dielectrophoresis for cell separation. The developed numerical model, along with all the equations involved, is discussed. The third chapter chapter describes the developed numerical model, along with all the equations involved in the modelling of the hybrid inertial spiral microfluidic device used for CTC separation. Additionally,

the technique used for the modelling of the cell is also reviewed. The verification and validation of the model are also discussed in this chapter. The fourth chapter presents the results of the investigation conducted for the separation of CTCs from blood cells. The effects of sheath flow, AC voltage, throughput, and the number of electrodes on cell separation are discussed. The migration characteristics of CTCs are also presented. Finally, the effectiveness of the channel to separate CTCs from a mixture of different subtypes white blood cells (WBCs) is also discussed. And the last chapter summarizes the results of the experiments and discusses the potential of the microfluidic device for CTC separation.

CHAPTER 2: RELATED THEORY

2.1 Inertial Migration of Cells

Inertial microfluidics operates in a laminar flow regime with finite inertia where nonlinear, irreversible yet predictable motions of the fluids are observed. This regime falls between the stokes flow where the inertia of the fluid can be ignored and the inviscid flow where turbulence is present [25]. This intermediate flow regime gives rise to several inertial effects including the inertial migration of the particles and secondary flow in a curved channel. Inertial migration of the particles is primarily brought about by two opposing forces: shear gradient lift force and wall-induced lift force. In the presence of curvature within the channel, particles are influenced by the dean drag which gives rise to the secondary flow in the channel. Additionally, particles are acted upon by viscous drag which causes them to accelerate to the same velocity along the flow direction of the fluid. These forces can be manipulated, and cell separation can be enhanced by the understanding of the underlying physics that causes the cells to equilibrate to their focusing positions due to the deterministic nature of the flow [36].

In the pressure-driven Poiseuille flow, the parabolic velocity profile across the cross-section of the spiral channel gives rise to the shear-induced inertial lift on the particles. The asymmetry of the relative velocity on the two sides of the cell causes a pressure difference generating a lift force that is directed away from the center of the channel. On the other hand, when the cells move towards the channel wall, the asymmetric wake of the cell near the wall gives rise to the Wall Induced Lift force. This force repels the cells away from the wall and towards the center of the channel. In a microfluidic channel, the randomly dispersed cells migrate to their

lateral equilibrium position in a narrow band by the counteraction of these two lift forces [37]. The net inertial lift force varies along the cross-section of the channel and can be expressed as [19]:

$$F_{Lift} = \frac{\rho_f v_m^2 a_p^4}{D_h^2} f_L(Re_c, z) \quad (1)$$

where, ρ_f is the fluid density, v_m is the maximum velocity of the fluid, a_p is the cell diameter, D_h is the hydraulic diameter of the channel, and f_L is the lift coefficient, which is a function of the Reynold number Re_c as well as the vertical position of the cell within channel *z*. The equilibrium position is a stationary point in a dynamic system where $f_L = 0$. For the fluid viscosity of μ_f, the Reynold number is given as:

$$Re_c = \frac{\rho_f v_m D_h}{\mu_f} \quad (2)$$

Due to the presence of curvature within the spiral microchannel, the difference in momentum near the channel centerline and the near-wall region induces the secondary flow. The fluid elements near the channel centerline are faster and thus have larger inertia than fluid near the channel walls, and would tend to flow outward around a curve, creating a pressure gradient in the radial direction of the channel. Because the channel is enclosed, relatively stagnant fluid near the walls re-circulates inward due to this centrifugal pressure gradient, creating two symmetric counter-rotating vortices, called the dean vortex. For a curved channel with a radius of curvature *R*, the qualitative features of these vortices are characterized by the dimensionless Dean number, De, which can be expressed as [38]:

$$De = Re\sqrt{\frac{D_h}{2R}} \quad (3)$$

The average dean flow velocity is a function of the dean number and is expressed by the equation [38]:

$$v_{dean} = 1.8 \times 10^{-4}\, De^{1.63} \qquad 4$$

The dean vortex enhances the lateral motion of cell across the channel and alters inertial focusing equilibrium positions by imposing a drag force, proportional to the Dean flow velocity [39]. The sedimentation force can be expressed as $F_{Sedim} = \frac{4}{24}\pi a_p^3 g(\rho_p - \rho_m)$, where ρ_p represents the density of the cells, and ρ_m is the density of the medium in which the cells are suspended. As the density of cell ρ_p = 1070 kg/m^3 is close to the medium density ρ_m = 1000 kg/m^3, the sedimentation force is considered to be negligible in this case [40]. Other forces such as Brownian, and Basset forces can also be ignored due to their negligible effects on the flow [33].

2.2 Migration of cells in the presence of Electric Field

With the addition of the DEP force, the dean drag enhances the separation distance between the cells of overlapping size. The location and number of the stable equilibrium positions of the cells are determined by the combined action of the inertial lift force, secondary flow drag, and DEP force. Dielectrophoresis exploits nonuniform electric fields to exert a force on cell suspended in a liquid medium. The magnitude and direction of the time averaged DEP force, $\boldsymbol{F_{DEP}}$, in an AC electric field depends on the respective polarizabilities of the cell and the suspension medium in the electric field, which in turn depend on their dielectric properties and the field frequency. This can be expressed mathematically as [41]:

$$\boldsymbol{F_{DEP}} = 2\pi\varepsilon_{med} r^3 Re[K_{CM}(f)]\nabla|\boldsymbol{E}|^2 \quad (5)$$

, where ε_{med} is the permittivity of the suspension medium, r is the radius of the cell, and f is the field frequency and $|\boldsymbol{E}|$ is the root-mean-squared intensity of the applied electric field. In the equation, $Re[K_{CM}(f)]$ represents the magnitude of the real part of the Clausius-Mossotti (CM) factor. CM factor can be mathematically expressed by the following equation [42]:

$$K_{CM}(f) = \frac{\bar{\varepsilon}_{cell} - \bar{\varepsilon}_{med}}{\bar{\varepsilon}_{cell} + 2\bar{\varepsilon}_{med}} \quad (6)$$

, where the complex permittivity of the cell and medium are given by $\bar{\varepsilon}_{cell}$ and $\bar{\varepsilon}_{med}$ respectively. The CM factor reflects the polarizability contrast between the cell and its suspension medium, and it is dependent on the frequency of the applied field. CM factor determines both the magnitude and direction of the DEP force. Positive DEP (pDEP) refers to the state when the particle is more polarizable than its immersion medium (i.e. $Re[K_{CM}(f)] > 0$). At this stage, the particle is attracted to the electrodes. On the other hand, Negative DEP(nDEP) corresponds to the state when the particle is less polarizable than its immersion medium (i.e. $Re[K_{CM}(f)] < 0$) and the particles are repelled from the electrodes. Between the positive and negative DEP there exist a point where no DEP force acts on the particle. This frequency is called the cross-over frequency.

$$\bar{\varepsilon} = \varepsilon - j\frac{\sigma}{\omega} \quad (7)$$

In Eqn. 7, for a cell of permittivity and conductivity ε and σ respectively, suspended in an electric field of angular frequency ω, the complex permittivity can be expressed by the following equation [42]:

$$\bar{\varepsilon}_{\text{mix}} = \bar{\varepsilon}_{\text{med}} \left(1 + 3\phi \frac{K_{CM}(f)}{1 - \phi K_{CM}(f)}\right) \quad 8$$

The permittivity of the medium changes in the presence of the cells and the Maxwell-Garnett equation can be used to find the new permittivity of the mixture, $\bar{\varepsilon}_{\text{mix}}$, which depends on the CM factor and the volume fraction, ϕ, of the suspended particles.

CHAPTER 3: OPERATING PRINCIPLE

3.1 Channel Description

In the proposed technique, planar interdigitated electrodes are patterned at the bottom of the spiral channel, and an AC electric field matching the cross-over frequency of the CTCs is applied. The spiral microchannel consists of two inlets and two outlets measuring 1mm. The spiral design shown in Figure 3.1 is formed by combining an inner semi-circle with a diameter of 4.5mm and a parametric equation of $r = (4.5 + \theta/\pi)$mm with θ ranging from π to 3.5π. The equation of the spiral has been derived from the work of Hou et al. [43]. Two primary design constraints influence the height of the channel. Firstly, the DEP force sets an upper limit on the channel's height. As the DEP force weakens from the electrode surface at the channel's bottom, it becomes insignificant at heights greater than 25 µm. To eliminate the bottom focusing position caused by particle inertial migration at 0.2 and 0.8 channel height, the channel's maximum height should be less than five times this value. Furthermore, the cell diameter to height ratio (a_p/H) significantly impacts the dean drag experienced by particles in a curved microchannel. If a_p/H > 0.07, strong inertial forces act on the cells, causing them to migrate and focus towards the inner wall of the channel. On the other hand, if a_p/H < 0.07, the dominating dean drag force results in particle circulation within the dean vortex. Additionally, decreasing the channel's height also reduces the achievable flow rate for the device. Considering these factors, the height of the spiral microchannel was determined to be 100 µm. The CTCs having a diameter of 14 has a_p/H > 0.07 and undergoes inertial focusing in the channel and will be focused towards the innerwall of the channel. Addtionally, to maintain the hydraulic diameter, and consequently Reynolds, and Dean numbers, the channel's width was set at 300 µm. The spiral channel is connected to the outlet by a straight section of 3.5mm. Of the two inlets, the sample of WBCs and CTCs mixture is applied through

the outer inlet and the sheath flow through the inner inlet. The sheath flow is pumped into the channel at twice the flow rate as the sample to displace all the particles towards the outer wall. An additional sheath flow is applied into the channel through the top half of the particle inlet to push all the particles to the bottom half of the channel required for the operation of the electrodes. The electrode width and gap are 100 μm and 20 μm respectively.

When the AC electric field is absent, it is expected that all cells would move towards the inner wall as they travel through the channel by the action of the dean vortex flow dynamics and inertial forces. When the AC electric field is applied, the resulting non-uniform electric field gives rise to the DEP force that would decrease sharply with the height of the channel. It is expected that no significant DEP force would act on the cancer cells at the cross-over frequency whereas the normal blood cells will be pushed vertically upwards by the interdigitated electrodes placed at the bottom of the channel. Additionally, the cells will be acted upon by the inertial lift force and dean drag force in a spiral microchannel. The combination of these forces will determine the equilibrium position of the cells. This is exploited to form separate streams of cells which can be collected at different outlets, effectively separating the cancer cells from the blood cells despite their size similarity.

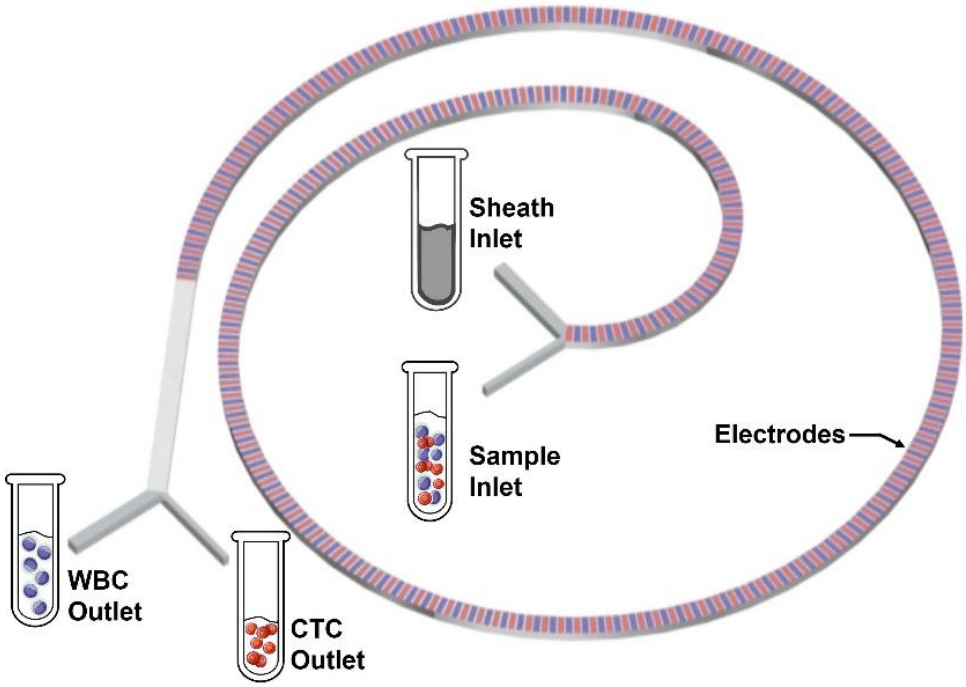

Figure 3.1 *Schematic of the DEP-inertial microfluidic device (Bottom view) for overlapping sized cell separation. Interdigitated electrodes are placed at the bottom of the microchannel. Cell samples and sheath fluids are pumped through the outer and inner inlet respectively. The cells are separated as they pass through the channel and are collected at the outlet based on the flow characteristics and electric field strength.*

3.2 Modelling of cells

The different components constituting an actual cell such as cytoplasm, nucleus, and cell membrane give rise to their inhomogeneity. To characterize this inhomogeneity single-shell model is used, with equivalent complex permittivity of the cell expressed as [44]:

$$\bar{\varepsilon}_{\text{cell}} = \bar{\varepsilon}_{\text{m}} \frac{\left(\frac{r}{r-d}\right)^3 + 2\left(\frac{\bar{\varepsilon}_i - \bar{\varepsilon}_{\text{m}}}{\bar{\varepsilon}_i + \bar{\varepsilon}_{\text{m}}}\right)}{\left(\frac{r}{r-d}\right)^3 - \left(\frac{\bar{\varepsilon}_i - \bar{\varepsilon}_{\text{m}}}{\bar{\varepsilon}_i + \bar{\varepsilon}_{\text{m}}}\right)} \qquad 9$$

where d is the cell membrane thickness, and the subscripts i and m stands for cytoplasm and cell membrane respectively. $\bar{\varepsilon}$ can be found from the Eqn. 7.

Lung cancer cell A549 is chosen as the representative of CTCs. On the other hand, WBC can be mainly categorized into four categories: Granulocytes, T-Lymphocyte, B-Lymphocyte and Monocyte. Different types of WBCs, their membrane capacitance and the approximate percentage in adults are given in Table 3.1.

Table 3.1 *Types of WBC, their size, total membrane capacitance and the approximate percentage in adults [45], [46]*

	Granulocytes	T-Lymphocyte	B-Lymphocyte	Monocyte	A549
Cell radius (μm)	4.71 ± 0.23	3.29 ± 0.35	3.29 ± 0.26	4.63 ± 0.36	6.9 ± 1.1
Membrane capacitance ($mF.m^{-2}$)	11 ± 3.2	11 ± 1.1	12.6 ± 3.5	15.3 ± 4.3	24.6 ± 2.7
Cross over frequency (kHz)	226	326	327	231	80
Percentage in adults	65	21	9	5	-

Despite all the variations among the WBCs, there is a significant margin of difference in the dielectric properties of the CTCs and WBCs which allows them to be separated by the action of DEP force. For instance, A549 has a total membrane capacitance of 24.6 ± 2.7 $mF.m^{-2}$ whereas the membrane capacitance of the WBCs is usually less than 20 $mF.m^{-2}$ [45]. The membrane capacitance is inversely proportional to the crossover frequency [35]. It can be seen from Table 3.1 and Figure 3.2 that the crossover frequency of the CTCs is significantly smaller than the crossover frequency of WBCs [17]. Given that the method proposed in this article relies on the relative difference in the crossover frequency of different cells for the separation, it can be expected to successfully separate CTCs from a mixture of WBCs. To demonstrate the working principle of our device and its effectiveness in the separation of overlapping-sized WBCs from the CTCs,

Granulocytes have been used since i) they have size overlaps with CTCs (A549) [46], [47]and ii) they make up the largest portions of the WBCs found in an adult body [46].

Table 3.2 *Properties of the cells used in the simulations a buffer conductivity of 0.055 S/m and a relative permittivity of 80. Granulocytes are considered for the representatives of the WBCs [15,32,33]*

	r (μm)	σ(S/m)	ε	d(nm)	σ_m(S/m)	ε_m
Large WBCs	6 ± 2	0.72	111	5	1×10^{-6}	5.5
A549	6.9 ± 1.1	0.23	100	5	2×10^{-6}	9.4

The properties of the cells that are being used in the numerical studies are summarized in Table 3.2. Assuming a buffer conductivity of 0.055 S/m and a relative permittivity of 80, the crossover frequencies for the CTCs and the WBCs have been obtained from the computations of the real part of the CM factor using Eqns. 6 and 7 and the cell properties listed in Table 3.2. At these conditions, WBC and CTC experience only one crossover frequency each, as shown in Figure 3.2, which gives the real part of the CM factor at a range of frequencies. From the figure, it can be seen that A549 has a crossover frequency of around 80 kHz whereas the crossover frequency of all the different types of WBCs is higher. When an AC field is applied at 80 kHz, the A549 cells will not experience any DEP force whereas the WBCs will experience a negative DEP force which will change their equilibrium position and assist in their separation from the A549 cells.

The general uncertainty in the crossover frequency of the A549 is reported to be ± 11% [45]. It can be seen from the thick purple line in Figure 3.2 that the real part of the CM factor of WBC stays nearly constant at approximately -0.4 over the CTC crossover uncertainty range. This

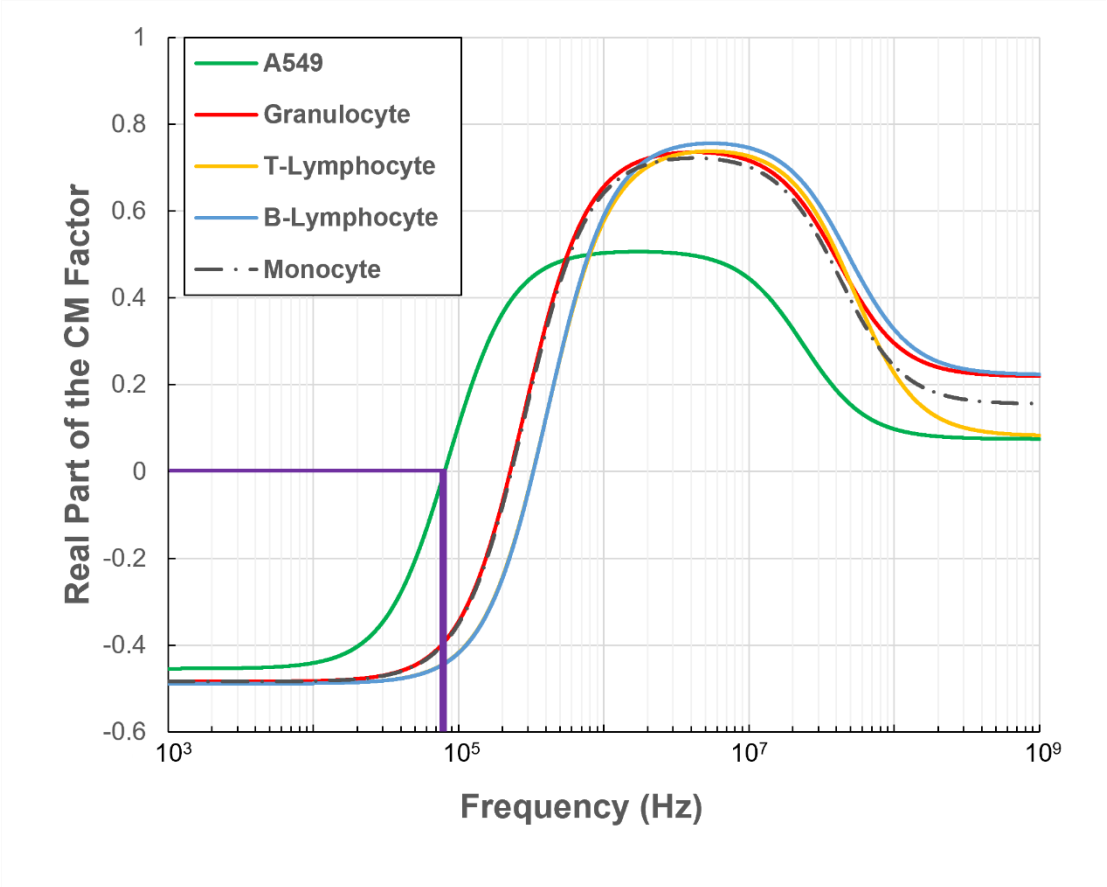

Figure 3.2 *Variation in the Real part of Clausius-Mossotti factor with the applied field frequency for both CTC and WBC. The purple line represents the crossover frequency of the CTC A549 cells. The thickness of the line represents the 11% uncertainty in it's value*

suggests that the strength and direction of the DEP force acting on WBCs will not significantly vary. Therefore, the general trend and the characteristics of the results are expected to remain relatively unchanged for the range at which the crossover frequency of the A549 cells is found.

3.3 Flow field and Electric field

The effectiveness of the overlapping size cell separation capability of the proposed hybrid system is evaluated using numerical simulation in Comsol Multiphysics. The steady-state velocity, pressure and electric field are obtained using stationary studies. Following that, a time-dependent study is carried out to determine the resulting cell trajectories. To obtain the velocity and pressure field, the incompressible Navier-Stokes equation is solved using the Laminar flow module ignoring the buoyancy and gravity effect as follows:

$$\rho\left(\frac{\partial \boldsymbol{v}}{\partial t} + \boldsymbol{v}\nabla\boldsymbol{v}\right) = -\nabla p + \eta\nabla^2\boldsymbol{v} \tag{10}$$

where $v, t, p,$ and η are velocity, time, pressure and viscosity, respectively. While discretizing the fluid domain, second-order elements are used for both the velocity components and the pressure field to obtain the effects of the shear gradient acting on the particles. No-slip boundary conditions at the walls and static pressure at the outlet are applied. The inlet velocities are then set to obtain the desired channel Reynolds number. On the other hand, the following set of equations are solved to obtain the electric field $\boldsymbol{E}$:

$$\boldsymbol{E} = -\nabla\phi_e \tag{11}$$

$$\nabla.(\epsilon_m \boldsymbol{E}) = \rho_E \tag{12}$$

$$\frac{\partial \rho_E}{\partial t} + \nabla.(\sigma \boldsymbol{E}) = 0 \tag{13}$$

, where ϕ_e, ε_m, ρ_E and σ are the electric potential, medium permittivity, volumetric free charge density and medium conductivity, respectively. Electrical potentials from 0 to 30V (peak-to-peak) were used as boundary conditions for the electrodes placed at the bottom of the microchannel. Alternating positive and negative potentials are applied at the consecutive electrodes and insulated boundary conditions are applied at the gap between electrodes. The obtained velocity, pressure and electric fields are shown in Figure 3.3.

(a)

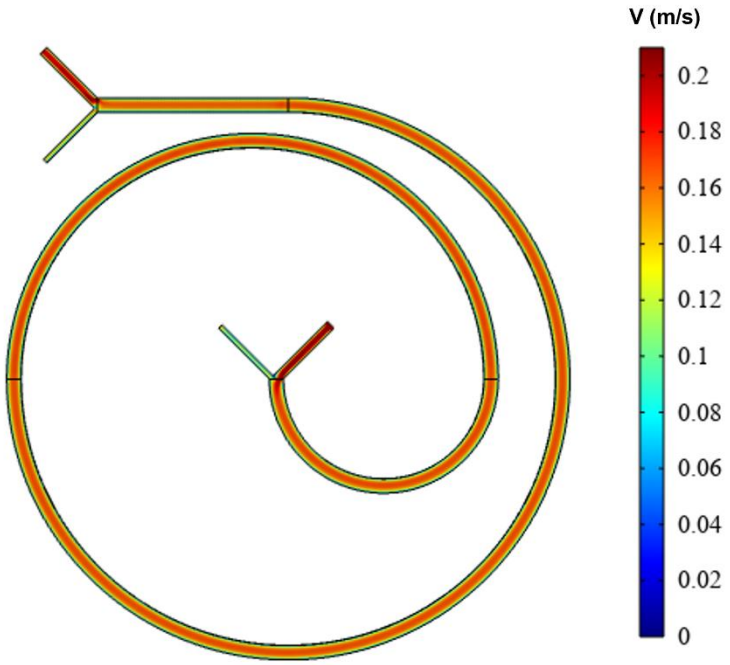

(b)

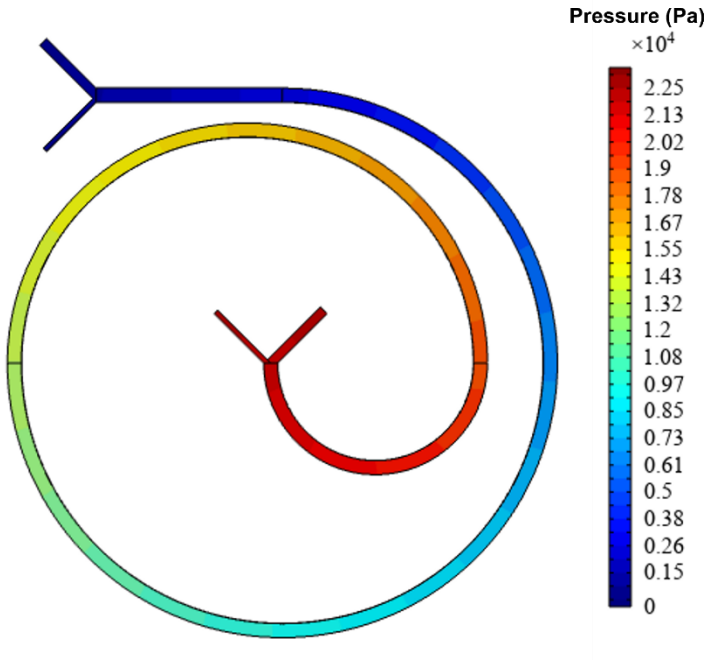

(c)

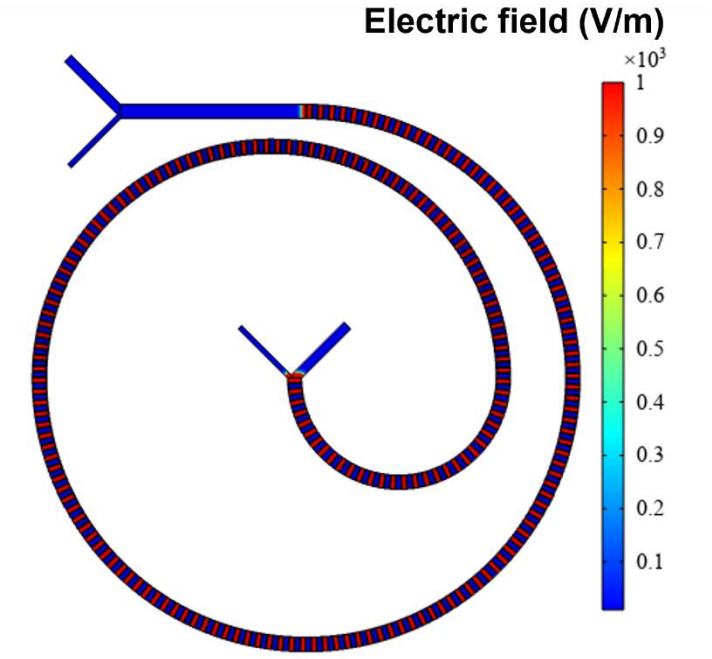

Figure 3.3 *In the first stage of this numerical simulation the the (a)velocity,(b) pressure and (c) electric fields are solved. With the solution of these field, Newton's second lawis computed to track the trajectory of the particles from the inlet to the outlet. The results shown here corresponds to a Reynols number of 40 and voltage of 7.5V.*

3.4 Particle Trajectory

After obtaining the laminar flow field and electric field strength, the effect of the resultant field on individual cells is provided by the particle tracing model. The motion of the cells is determined by the primary forces acting on them, namely, the inertial lift, the drag and the DEP force. The resulting cell particle trajectories are provided by Newton's second law of motion incorporating the above-mentioned forces in an incompressible medium as follows:

$$m_{cell}\frac{d}{dt}(\boldsymbol{v_{cell}}) = \boldsymbol{F_{drag}} + \boldsymbol{F_{lift}} + \boldsymbol{F_{DEP}} \quad (14)$$

For the computations of the drag force at intermediate Re number, the Schiller-Naumann drag model is used [48]. This model accounts for inertial effect of the drag force acting on a single spherical particle [49]:

$$F_{drag} = \left(\frac{1}{\tau_p}\right) m_{cell}(\boldsymbol{v} - \boldsymbol{v}_{cell}) \quad (15)$$

The velocity response time, τ_p is defined as:

$$\tau_p = \frac{4\rho_p a_p^2}{3\mu C_d Re} \quad (16)$$

, where the drag coefficient $C_d$can be expressed as[49]:

$$C_d = \frac{24}{Re}(1 + 0.15Re^{0.687}) \quad (17)$$

The lift force is computed with respect to the walls using Eqn. 1 and the dielectrophoretic force is computed using Eqn. 5. In accordance with the existing literature single-shell model is used to characterize the inhomogeneity that arises due to the presence of different components cells such as cytoplasm, nucleus, and cell membrane constituting an actual cell [44]. Ten cells of each type are released from the inlet at an interval of 2×10^{-5} s with injection starting from 0 s. Bounce wall condition is applied at the wall for the cell particles. To avoid stiffness in the numerical solutions, an automatic time-stepping method known as Generalized alpha has been utilized. The interval between the cell injection time was maintained to be a multiple of this time step. The total time for simulation is set to 0.5s which is determined by the time it takes for the particles to reach the outlet from the inlet. In the time-dependent study, a fully coupled iterative GMRES solver is used with a convergence criterion of 10^{-3}.

3.5 Verification and Validation

A mesh sensitivity analysis is performed following the guideline presented by Roache [50] with three levels of mesh resolution. Comparing the two finer grids, the grid convergence index (GCI) is calculated using Eqn. 18. A GCI of 0.198% is obtained in our study with a safety factor of 1.25. Within 95% confidence interval, it can be stated that there is a negligible difference between the results obtained using elements of average size 0.0148mm and 0.0129mm grid with 523,734 and 781,080 elements, respectively. The grid study showed that with the current mesh setting the solutions of the numerical simulations that followed are independent of the grids [50].

$$GCI_{21} = F_s \frac{e_{21}}{r_{21}^{p} - 1} \qquad 18$$

(a)

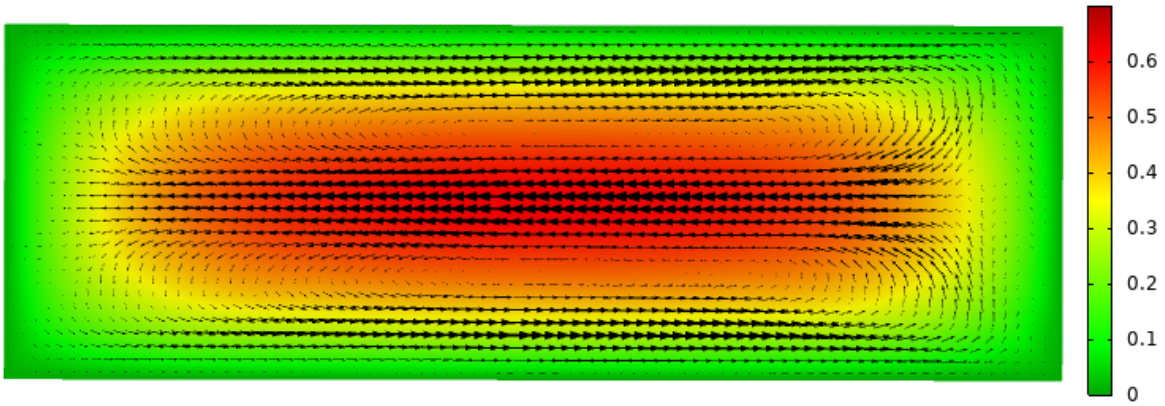

(b)

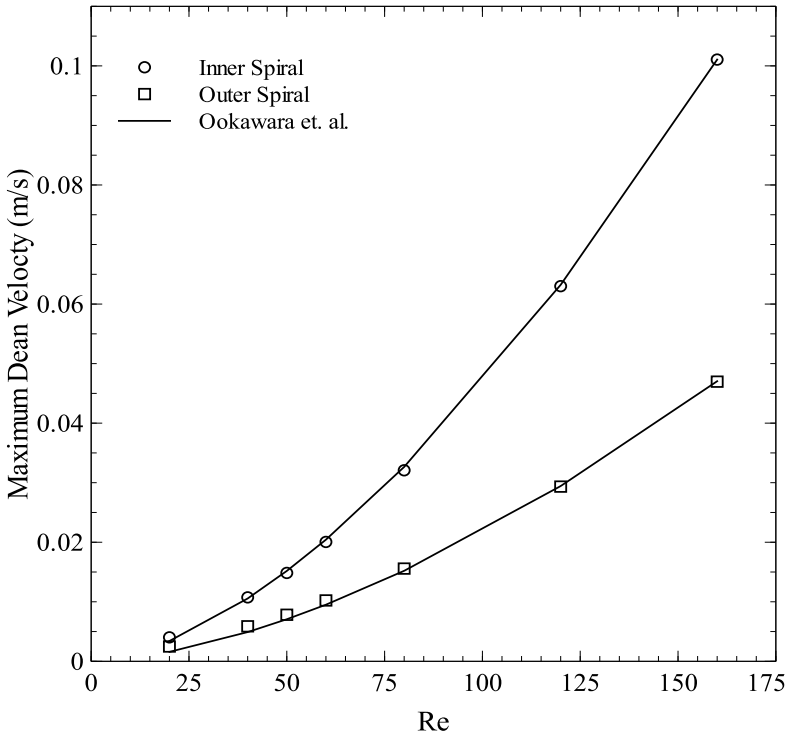

Figure 3.4 *The numerical model that has been used in the study has been validated against the experimental works existing in the literature. Dean velocity obtained in our study at different Reynolds numbers are in good agreement with the empirical relation propose. (a) Shows the dean velocity contour (b) comparison of the dean velocity obtained in our simulation with the experiemenal work of Ookawara et. al. [38]*

The presence of curvature in the spiral microchannel gives rise to the dean vortex which is a crucial phenomenon that controls the cells' migration and focusing characteristics within the fluid domain. To verify the inertial flow model in this study, the maximum dean velocity that we obtained is compared with the experimental results of Ookawara et. al. [38]. For the purpose of comparison, the spiral microchannel has been assumed to be comprised of two circular sections of radius 2.25cm and 4cm. As shown in Figure 3.4, the maximum dean velocities are represented by circle marks for the inner spiral (smaller circular section) and square marks for the outer spiral (larger circular section) at different Reynolds numbers. In Ookawara's work, an empirical power law equation was formulated between the average dean velocity and the flow Reynolds number as expressed by Eqn. 4. The value of the coefficient of proportionality was found to vary significantly with the change in the channel aspect ratio while the exponent was confirmed to remain unchanged. As illustrated in Figure 3.4-b, the numerical results obtained in our study are in good agreement with the empirical formulation. To validate our methodology on the electrical module of the simulation, we have compared our electric field distribution with the work of Zhang et. al. [51]. In Zhang's work, numerical simulations were used to augment the experimental results on particle separation using DEP force in a serpentine channel. Moreover, the electric field contour is illustrated in Figure 3.5 obtained from our simulation, is in good agreement with published results from [51]. Additionally, a particle at 10μm from the bottom of the electrode is found to experience a maximum vertical DEP force of 1.6×10^{-7} N based on our simulation, which compares well with 1.68×10^{-7} N demonstrated in the work of Zhang et. al. [51].

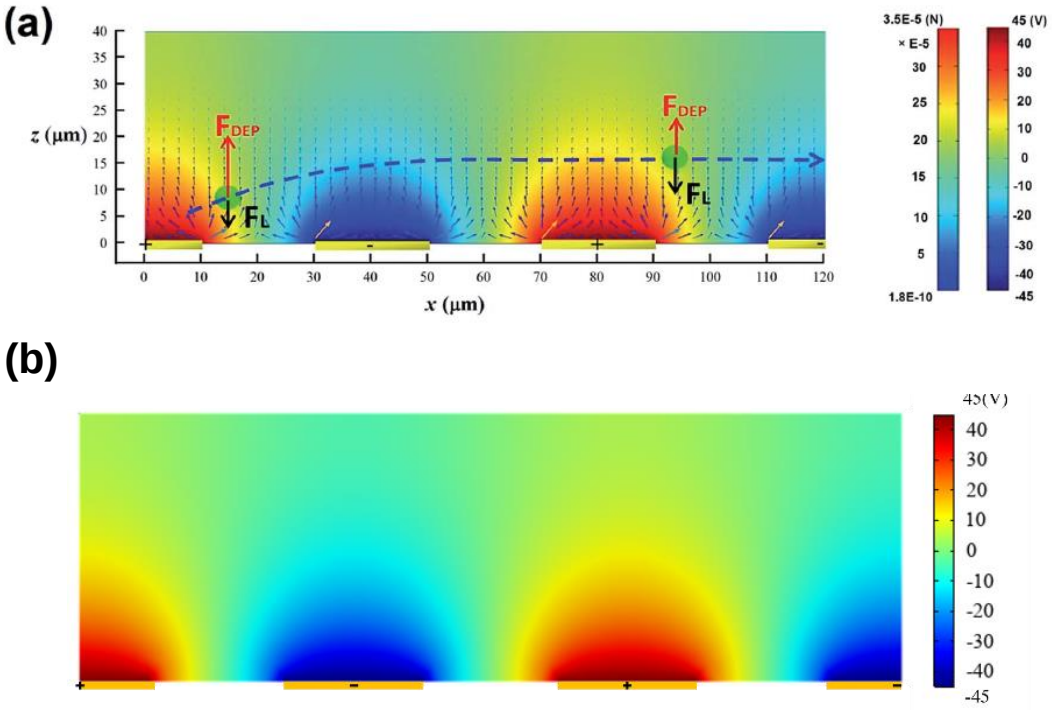

Figure 3.5 *The color map shows the electric field distributuion within a tongitudinal section of the channel at an electric field frequency of 1MHz. (a) Results from the work of Zhang et. al. [50] (b) Electric field contour obtained from our simulation*

CHAPTER 4: RESULTS AND DISCUSSION

In hybrid inertial microfluidic devices, the vital factors that influence the flow physics and particle trajectories are the electric field strength, flow regime and dielectric properties of the sample and the buffer. In this work, the influence of voltage and Reynolds number on the separation efficiency of the overlapping-sized cancer cells from healthy blood cells have been numerically investigated to determine the best separation scenario. In the following section, the effects of these parameters on the migration characteristics of the cells are discussed.

4.1 Effects of AC voltage on cell separation

The voltage and frequency of the applied electric field determine the focusing patterns (position and number) of the cells in the microchannel. To study the effects of AC voltage on cell migration, the investigation is carried out at different voltages at the cross-over frequency of the cancer cells.

The vertical displacements of the cells under increasing electrical voltage are illustrated in Figure 4.1 for a Reynolds number of 40. This is considered as the representative flow regime as a similar change in focusing characteristics with voltage is observed at other Reynolds numbers as well. For better visualization of the trajectories of the particles, a 3D isometric view of the outlet at three separate voltages is presented in Figure 4.1-a-c, where the green stream represents the cancer cells, and the red stream represents the white blood cells. When the applied peak-to-peak electrical voltage ($V_{p\text{-}p}$) is 0V, no DEP force acts on both cell types and it can be seen from Figure 4.1-a that they are coming out as a single stream at the outlet. Varying the applied voltage does

not change the trajectories of the CTCs, as can be seen from Figure 4.1. This is the consequence of the absence of any dielectrophoretic force on the CTCs in an electric field where the frequency of the applied voltage is set at the cross-over frequency of the cancer cells. On the other hand, increasing the voltage levitates the WBCs upward due to the negative DEP force they experience at the applied frequency. The WBCs transition from the bottom to the top focusing position at a voltage termed as the critical voltage as shown in Figure 4.1-b. For a Reynolds number of 40, the critical voltage is 7.5V. Below this voltage, both cell types are found to be focusing on a similar position from the bottom of the channel, as shown in Figure 4.1-a. On the other hand, above the critical voltage, all the white blood cells are found at the top focusing position due to higher negative DEP force, as can be seen in Figure 4.1-c. According to Eqn. 5, the DEP force is directly proportional to $\nabla \boldsymbol{E}^2$. Thus, it can be expected that as the voltage increases, the cells are expected to experience a higher DEP force. The variation in the vertical displacement of both WBCs and CTCs at peak-to-peak applied voltages ranging from 5V to 15V are shown in Figure 4.2. It can be seen from Figure 4.2, that above the critical voltage the vertical focusing positions of the cells remain constant with variation in voltage. The CTCs and WBCs focus at approximately 20 μm and 80μm, respectively, across the channel height. It can also be observed that with the increase in voltage above the critical value, the range over which the WBCs are distributed reduces to a very narrow and focused stream.

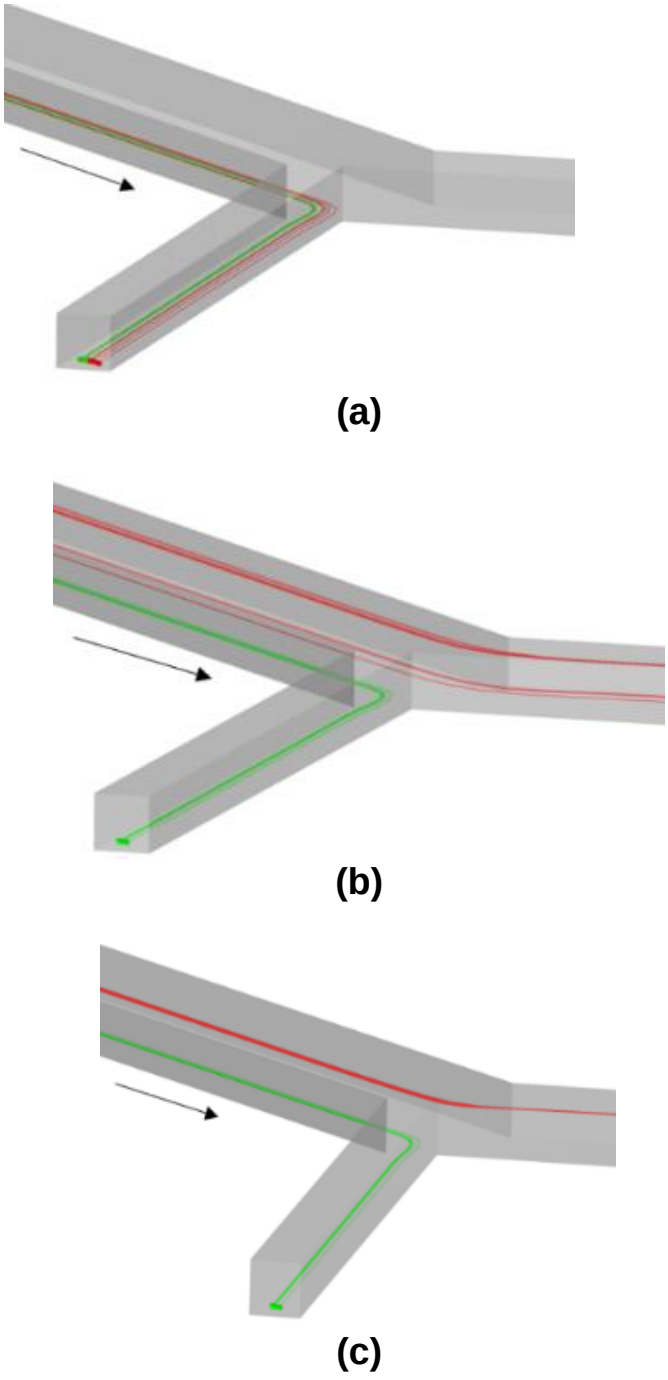

Figure 4.1 *The vertical separation of the cells at Re = 40 for voltage of (a) 0V (b) 7.5V and (c) 10V are shown in 3D outlet view. The red and green lines show the trajectories of WBC and CTC respectively. The black arrow shows the direction of the flow*

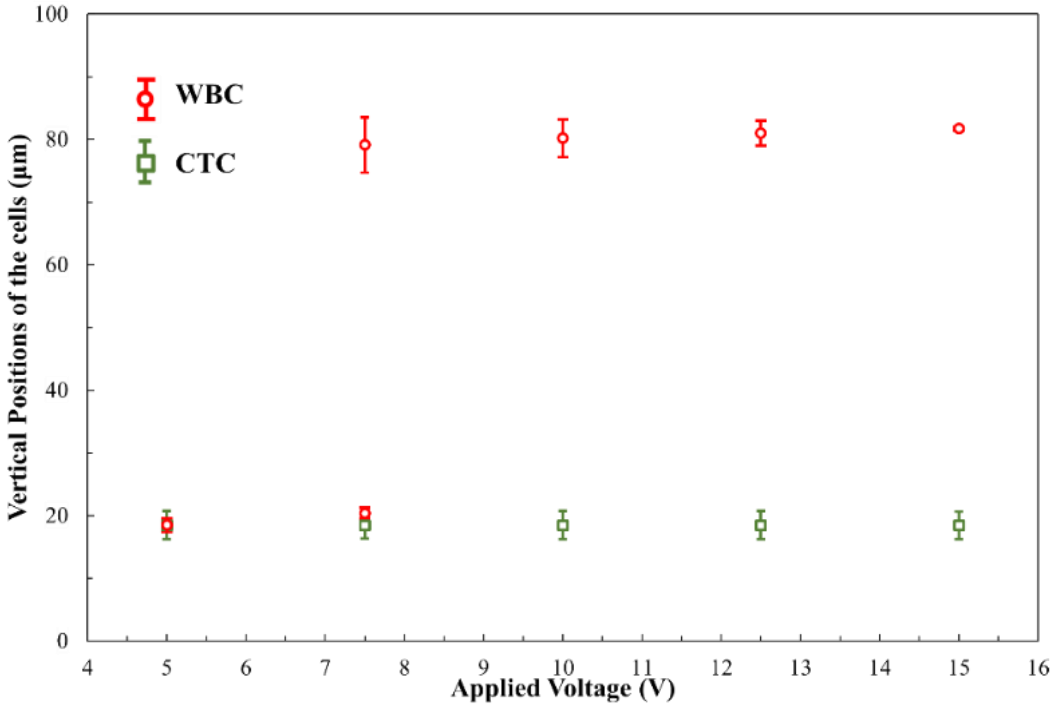

Figure 4.2 *The final vertical position of cells and their range at the outlet at different voltage has been summarized*

In addition to the vertical displacement, the WBCs are also displaced laterally between the inner and outer walls of the curved microchannel. Figure 4.3 shows the top view of the spiral microchannel where the particle trajectories over the length of the channel can be observed for a peak-to-peak voltage of 7.5V at a Reynolds number of 40. It can be seen from Figure 4.3 that both types of cells are injected through the outer inlet. CTCs move from the outer wall of the channel to the inner wall due to the dean vortices, whereas the white blood cells assume their initial trajectories. This forms two separate streams of particles and can be collected separately through the two outlets. The lateral separation distance between these two streams of particles is dependent on the applied voltage. As can be seen in Figure 4.4-a, when the applied voltage is 0V, both blood cells and the cancer cells form a single indistinguishable stream and are collected through the same

inner outlet. With the increase in the applied voltage, two separate streams of cells start to form where the CTCs can be seen to continue their initial trajectory whereas the WBCs are laterally displaced. The magnitude of this displacement increases with the applied voltage up to the critical voltage. For the Reynolds number of 40, the maximum lateral separation distance is achieved at the critical voltage of 7.5V, as can be seen in Figure 4.5. At 10V, the lateral separation distance between the two streams of the cell decreases again, as the green and the red stream come closer to each other as illustrated in Figure 4.4-c. Any further increase in the voltage reduces the lateral separation distance again as shown in Figure 4.5.

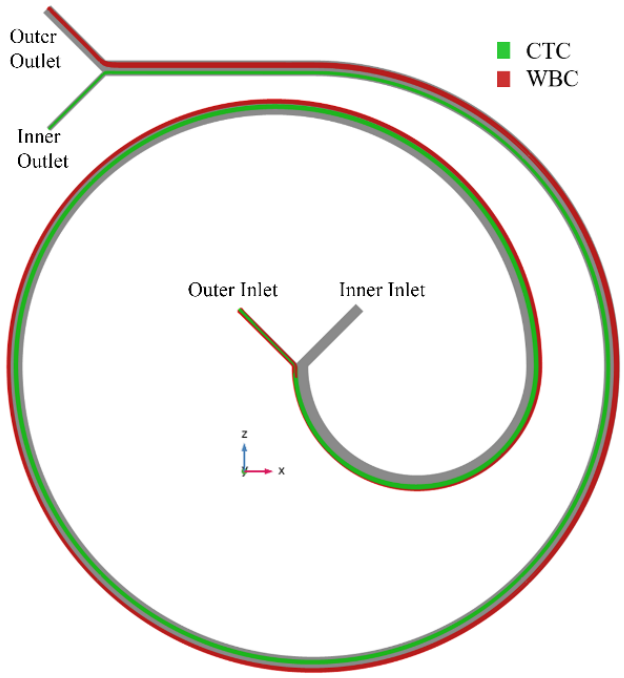

Figure 4.3 *The top view of the channel shows the lateral separation of the particles at Reynolds number 40. Mixture the CTCs and WBCs are injected through the outer inlet. The CTCs can be collected at the inner inlet towards the end of the channel.*

The lateral focusing position and width of the focusing stream at the outlet cross-section for applied voltage ranging from 5V to 15V are shown by the bars in Figure 4.5. It can be seen that

CTCs assume their initial focusing stream at various voltages. On the other hand, the lateral displacement of the WBCs is highly dependent on the applied voltage and reaches a maximum at the critical voltage. For a Reynolds number of 40 at the critical voltage of 7.5V, the maximum lateral separation distance of 120μm is achieved. Furthermore, it is also seen that at low voltages, the blood cells are found over a large range across the channel, but generally, the width of these lateral focusing streams decreases with the increase in the voltage.

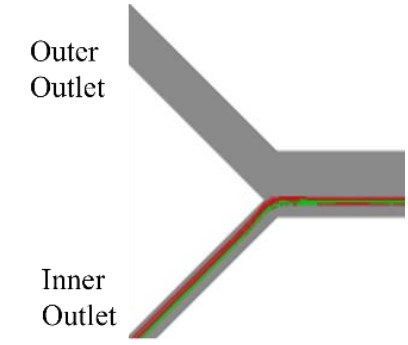

(a)

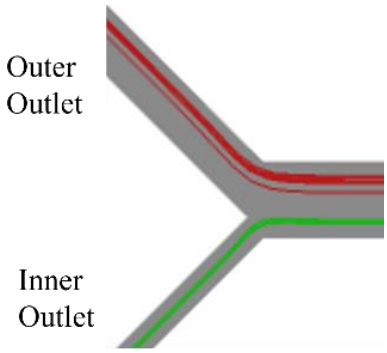

(b)

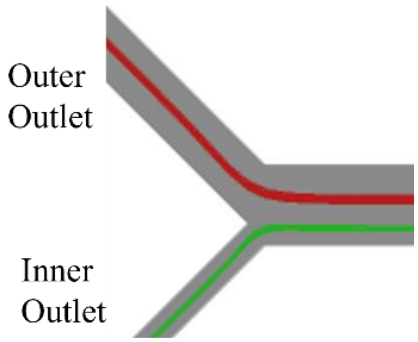

(c)

Figure 4.4 *As the particles travels through the channel, they are laterally separated based on the voltage that is applied. (a) When V = 0 all the cells are collected through the inner outlet. (b) When the voltage is near the critical voltage, 7.5V for Reynolds number 40, the lateral separation distance between the particles increases and they are collected in two separate outlets. (d) At voltage greater than the critical voltage (10V) the lateral separation distance decreases again.*

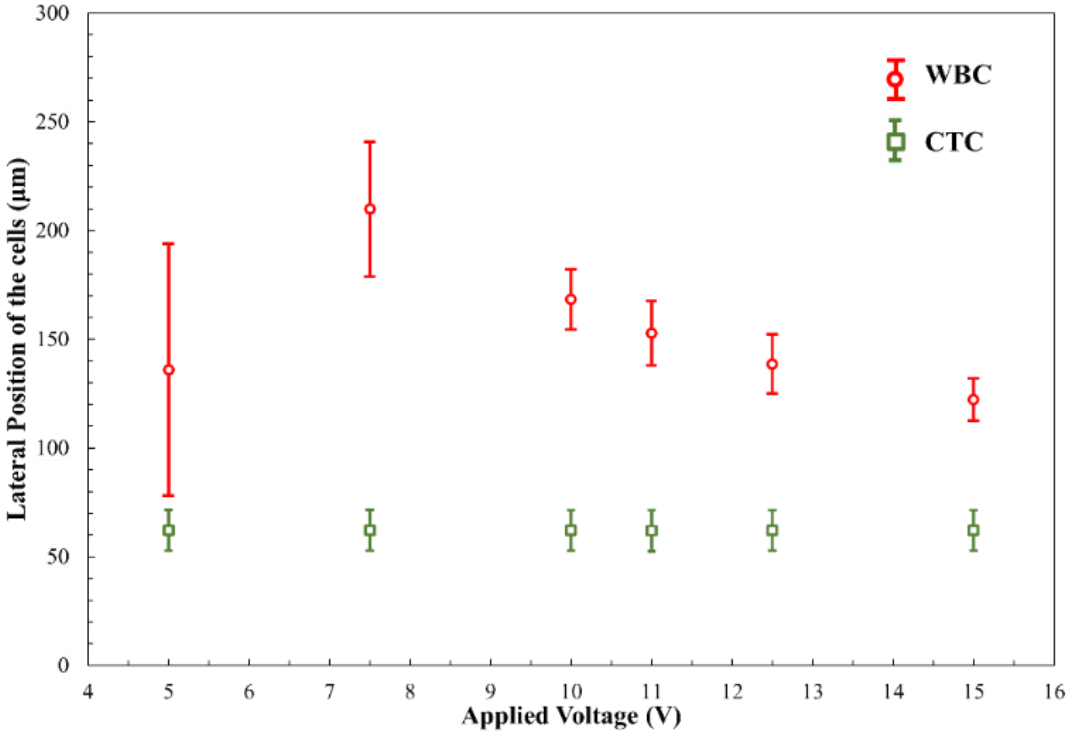

Figure 4.5 *In this figure the bar represents the lateral width of the focusing stream of the particles. As the voltage is increased, WBC starts to displace laterally up to a critical voltage, forming a separate stream of particles. After that the separation distance drops off again.*

4.2 Effect of Sheath Flow

In a microfluidic channel embedded with interdigitated electrodes at the bottom of the channel, the strength of the non-uniform electric field decreases exponentially from the vicinity of the electrodes. As the strength of the electric field diminishes near the top of the channel, a top sheath flow needs to be employed to eliminate the top focusing position of the cells and push them near the bottom for their successful separation. In this work, several buffer inlet configuration for the top sheath flow has been explored to study the impact of the sheath flow on the separation characteristics of the cells.

The results show that in the absence of any DEP force when the applied voltage is zero and at the vertical buffer flow inlet of 25 µm, cells are found at approximately 20 µm and 80 µm of the channel height. Thus, two separate streams are formed with an identical mixture of cells. The results for various buffer inlet configuration at 30V and at a Reynold number of 40 is shown in Figure 4.6. At 30V it is observed that all the WBCs were moved to the top focusing position but the CTCs were distributed evenly between the top and bottom focusing positions as shown in Figure 4.6-a. Thus no distinct stream of WBCs and CTCs is found and the cell could not be separated in this configuration.

When the vertical buffer flow inlet is 50 µm, the cell mixture is pushed to the bottom half of the channel. At this configuration and in the absence of any electric field, only one focusing position of the cells is found at approximately 20 µm from the bottom of the channel for both cell types, eliminating the top focusing position. As the voltage is increased, negative DEP force acts on the WBCs and they are pushed vertically upward. Owing to the dielectric properties of the CTCs no DEP force acts on them, hence the CTCs maintain their initial trajectory near the bottom

of the channel. At a voltage greater than the critical voltage, two distinct streams of cells are formed represented by the blue and the red lines in Figure 4.6-b. At vertical buffer flow inlet of 75 µm, the WBCs and the CTCs are separated both vertically and laterally when the applied voltage is 30V. This can be employed to collect the CTCs and WBCs through different outlets as shown in Figure 4.6-c. This configuration has been used for the subsequent investigation of the migration characteristics of the cells in this article.

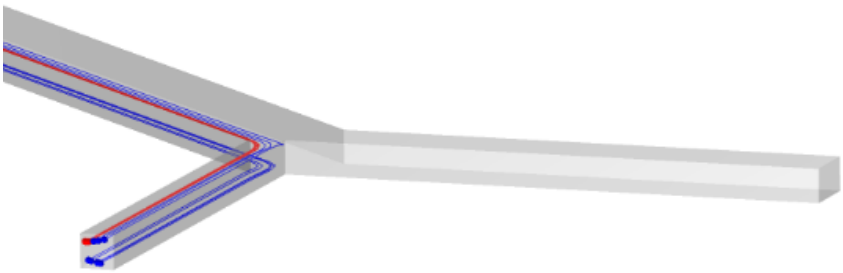

(a) Sheath = 0.25

(b) Sheath = 0.5

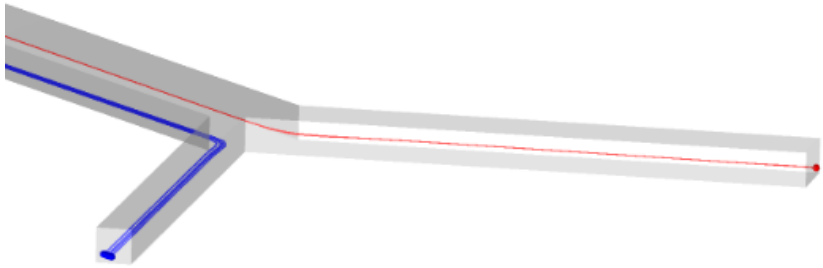

(c) Sheath = 0.75

Figure 4.6 *For an applied voltage of 30v the outlet positions of the cells with variation in the top sheath dimension [(a)0.25 (b) 0.50 (c) 0.75] are shown in the figure. The red stream represents the WBCs and the blue stream represents the CTCs.*

4.3 Migration Characteristics

The final focusing position of the particles is a consequence of the equilibrium between the DEP, lift, and dean forces. In this section, the behavior of these important forces that determines the focusing position is discussed. The relative direction in which these three forces act within the channel is shown in Figure 4.7-a. The plots in Figure 4.7-b-d have been obtained from the literature and show the relative magnitude of these forces, where the "y" axis represents the height axis of the channel for all three plots. The vertical nDEP force is always directed upwards and the average magnitude of this force decreases with the distance from electrodes at bottom of the channel. This is illustrated in Figure 4.7-b [51].

In the absence of any DEP force in a straight rectangular channel, particles are acted upon by the wall-induced lift force and shear gradient lift force. If the particles are close to the wall, the wall-induced lift force pushes the particle toward the center. On the other hand, due to the parabolic nature of the fluid velocity profile, shear gradient lift force pushes the particles away from the

center towards the walls. By the counteraction of these forces, two dynamic stable equilibrium positions are created in a straight rectangular channel. It can be seen in Figure 4.7-c that there are three positions at which the lift force becomes equal to zero[51]. The first and the last equilibrium coordinates are at approximately 0.2 and 0.8 fractions of the channel height, and these correspond to the focusing positions at which the cells can be found. On the other hand, the equilibrium position in the middle as shown in the figure is dynamically unstable and the particles are directed away from it, thus no cell focuses on this position. Additionally, in a curved channel, due to the centrifugal force on the fluid in motion, the particles at the center experience significant outward force, creating a low-pressure region at the center. Fluids from the top and bottom of the channel recirculate in this low-pressure region forming two symmetric, but counter-rotating vortices known as dean vortices giving rise to dean drag. The relative magnitude and direction of the horizontal component of this dean force are shown in Figure 4.7-d [52]. It can be seen in the figure that the magnitude of the horizontal dean force is larger towards the center of the channel when it is directed toward the outer wall. This dean force, in addition to the wall-induced and shear gradient lift forces, will make the two focusing positions found in a straight channel unstable. As a result, in a spiral microchannel, all the particles will focus vertically in the middle of the channel. In our work, once a top sheath flow has been applied, the focusing position in the spiral microchannel displaces vertically from the middle of the channel to around 0.2 fractions of the channel height from the bottom of the channel in the absence of any DEP force. When there is an additional DEP force acting on the particles in the spiral channel, it causes a change in the equilibrium positions of the particles both laterally and vertically.

As the voltage increases, the vertical DEP force increases, and the cells are repelled upward by the electrodes toward the center of the channel as discussed in the previous section. Towards

the channel center, the strength of the horizontal dean drag is higher as shown in Figure 4.7-d. As the particle moves vertically upwards towards the center of the channel, they are, simultaneously, displaced horizontally towards the outer wall by the dean drag. Consequently, with the increase in voltage up to the critical voltage, in addition to the vertical displacement, the blood cells also undergo lateral displacement whereas the cancer cells assume their initial trajectory as no DEP force acts on them.

Above the critical voltage, the blood cells can be found in the upper region of the channel and at this region, the horizontal dean force starts to decrease in magnitude as the particles move away from the center of the channel, as can be seen in Figure 4.7-c, and the inertial lift forces cause the particle to move towards the inner wall. The strength of the horizontal dean force in the outward direction decreases as the cells are moved towards the top wall. Consequently, as the WBCs are moved vertically upwards by the DEP force, the lateral focusing position move towards the inner wall, hence decreasing the separation distance again once the voltage is higher than the critical voltage.

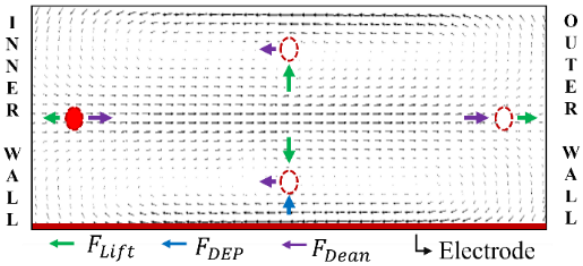

(a)

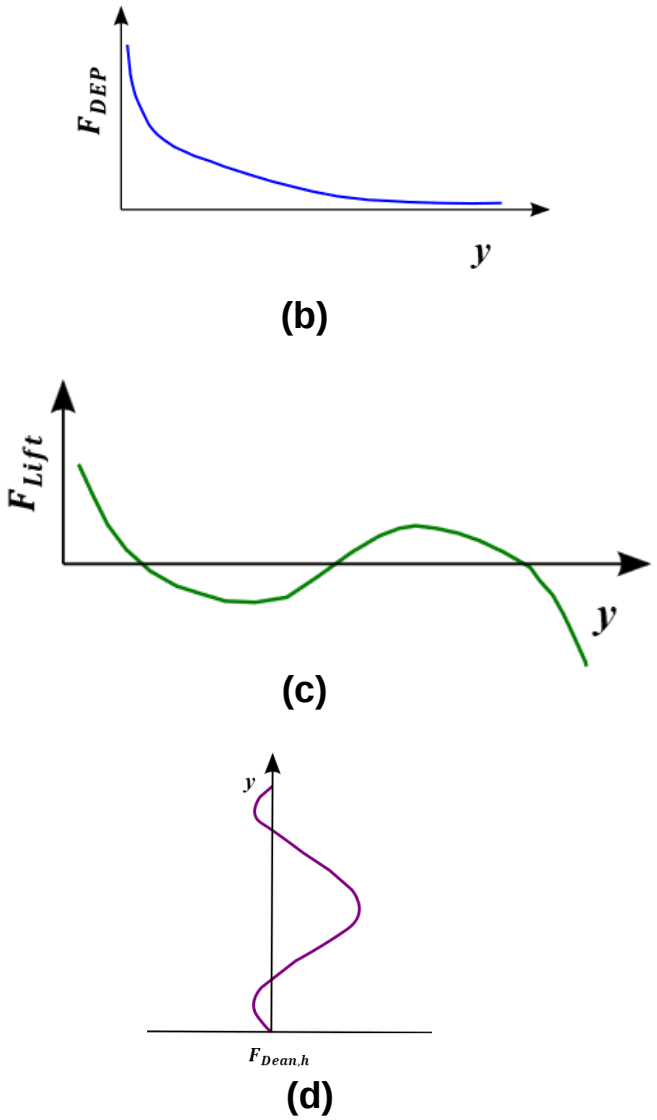

Figure 4.7 *The relative magnitude and direction of the three forces determine the particle trajectory in a hybrid DEP-inertial microfluidic channel. (a) Microchannel cross-sections illustrating the direction of the three forces and the migration for particles. The relative scaling of these three forces, as obtained from the literature, is demonstrated in the following plots (b) The vertical DEP force decreases with the increase in height from the electrode [51](c) The lift is the summation of the wall wall-induced force and shear gradient lift force [51](d) The Dean force in the horizontal direction is directed towards the outer wall in the center and towards the inner wall near the top and bottom wall [52].*

4.4 Effects of throughput on cell separation

In the previous sections, the change in the migration patterns of the cells with the variation in the electric field strength is discussed. It is found that the maximum lateral separation of the cells can be achieved when the applied voltage is equal to the critical voltage at the cross-over frequency of the cancer cells. Here, to better understand the relationship between the critical voltage and the Reynolds number, the effect of the flow rate in the DEP embedded hybrid inertial device is investigated at various Reynolds numbers. The Reynolds number is set to vary from 30 to 60, and the results are illustrated in Figure 4.8. At the applied frequency, the CTCs remain unaffected by any variation in the electric field and assume their fixed positions. Consequently, the positions of the CTCs at different Reynolds numbers remain unchanged at all the voltages. It is observed that with the variation in the voltage, only the WBCs change their position, and thus only their positions are illustrated at a various voltage (0-30V) at each Reynolds number.

In Figure 4.8, the green lines represent the focusing position and stream width of the WBCs at 0V, which approximates the focusing pattern of the cancer cells at all the voltages. The red lines represent the focusing positions and pattern of the WBCs at the critical voltage. The yellow stream represents the state of the WBCs at 30V, whereas the blue and the purple lines represent the focusing pattern of the WBCs at two other intermediate voltages. With the increase in Reynolds number, the particle stream at 0V, which also represents the cancer cells at all the voltages, is seen to be pushed towards the inner wall. Consequently, the distance between the green and the red streams of particles increases with the increase in the Reynold number.

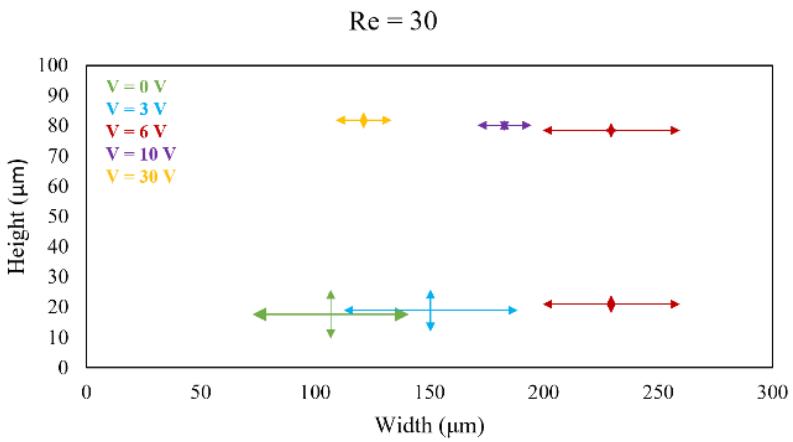
Re = 30
V = 0 V
V = 3 V
V = 6 V
V = 10 V
V = 30 V
Height (μm)
Width (μm)
0
10
20
30
40
50
60
70
80
90
100
0
50
100
150
200
250
300

(a)

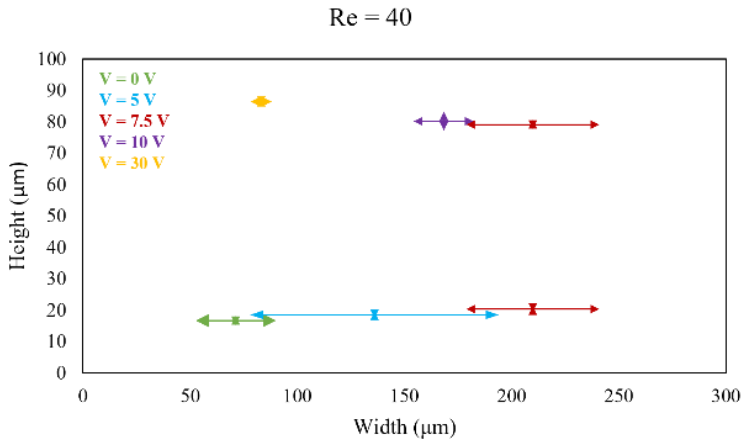
Re = 40
V = 0 V
V = 5 V
V = 7.5 V
V = 10 V
V = 30 V
Height (μm)
Width (μm)
0
10
20
30
40
50
60
70
80
90
100
0
50
100
150
200
250
300

(b)

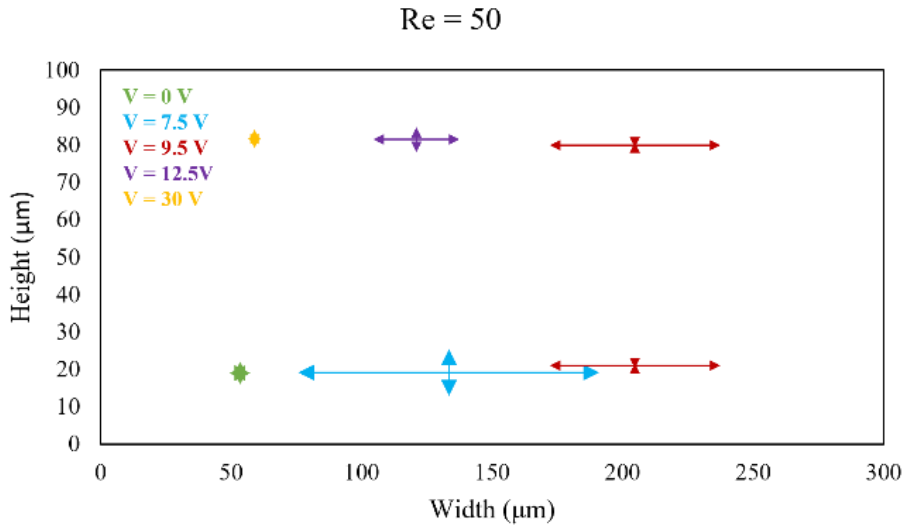

(c)

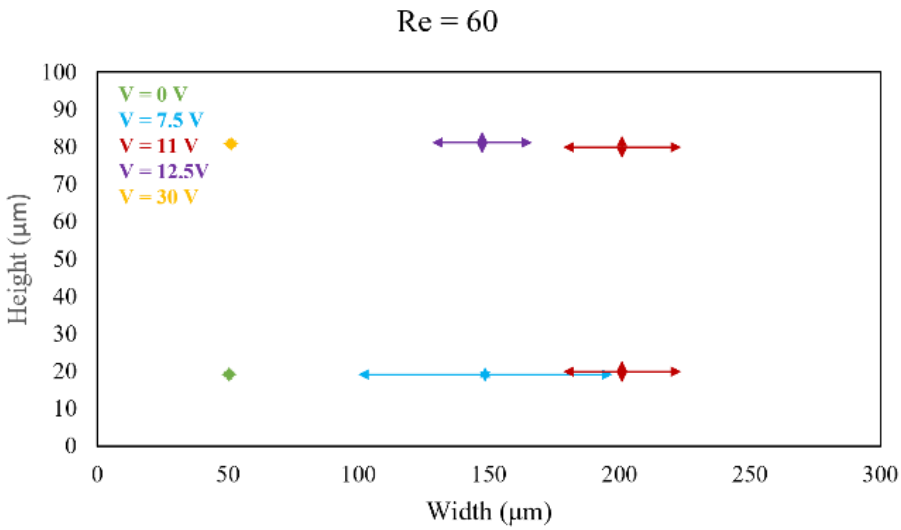

(d)

Figure 4.8 *Focusing position and stream width of WBCs at different Reynolds number and voltages have been represented by the arrow bars. Reynolds number has been varied from 30-60 in Fig. a-d. At each Reynolds number the distribution of the WBC at the outlet cross-section is illustrated by the arrow lines. The position of the CTC will be similar to the case with voltage = 0V and they will remain unaffected by the change in voltage and stay at the same position. (e) Maximum lateral separation distance can be obtained at the critical voltage for the separation at different Reynolds numbers. Both the separation distance that can be achieved and the voltage at which maximum separation of the stream between CTC and WBC occurs increases with the increase in Reynolds number.*

The lateral and vertical height at which the WBCs are collected at the outlet is shown in Figure 4.9. The CTCs have the same size as the WBCs, thus they are acted upon by the same inertial force, and hence they are observed to show a similar migration characteristic as WBCs at all the flow conditions in the absence of an electric field. Additionally, in the presence of an electric field, the CTCs do not change their position at the outlet and maintain their initial flow trajectory similar to the WBCs at 0V. As a result, the CTCs have been omitted from this figure.

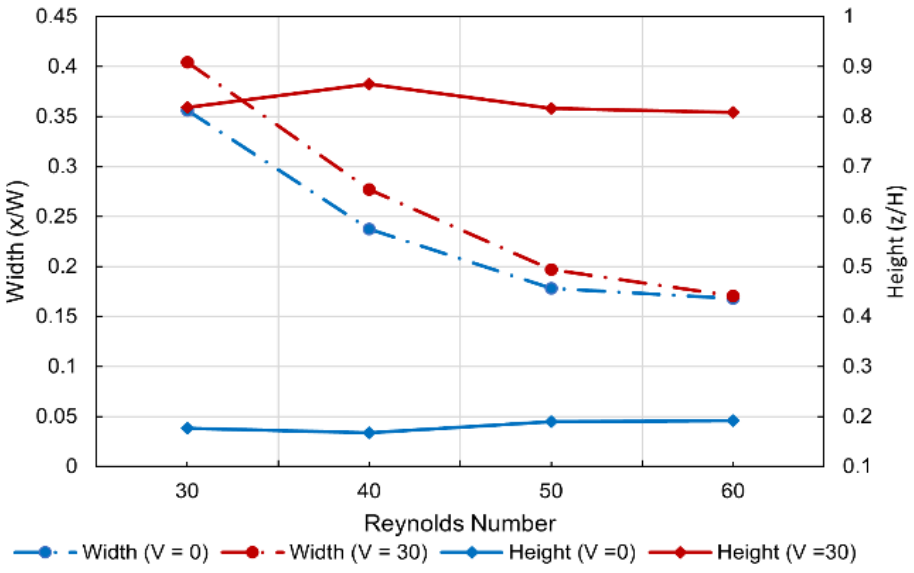

Figure 4.9 *The lateral and vertical position of the WBCs at the outlet with the variation in the Reynolds number at voltage 0 and 30v given by the blue and the red lines respectively*

As the Reynolds number is increased, all the particles are pushed towards the side wall of the channel from the center due to the increase in the inertial-lift force. This is observed both in the presence and in the absence of an electric field and shown by the dashed lines in Figure 4.9. Thus, with the increase in the Reynolds number, the lateral distance between the particles at the outlet decreases at 30V. However, it can be seen from the blue solid lines that the WBCs are found at the bottom of the channel when there is no applied voltage. In the presence of an electric field,

when the applied voltage is 30V, significant DEP force acts on the WBCs, and as discussed in the previous section, the WBCs can be collected from the top of the channel as shown by the red solid line. As shown by the two solid lines in Fig. 5, the heights at which the WBCs are collected at the outlet do not change significantly with the Reynolds numbers. Thus, two separate streams of cells can be collected at the outlet.

Additionally, it can be observed that as the Reynolds number increases the critical voltage at which the maximum lateral separation of the cells occurs increases, as shown in Figure 4.8 a-d. For Re = 30, 40, 50, and 60, the critical voltages are 6V, 7.5V, 9.5V and 11V, respectively. This is summarized in Figure 4.10. As the voltage is increased from the critical voltage, the separation distance is reduced again due to the decrease in the lateral distance between the streams. Thus, it can be concluded that with the increase in Reynolds number in the range of 30-60, the maximum lateral separation distance between the particles increases. In our spiral microchannel, a Reynolds number of 60 translates to a throughput of ~0.7 mL/min. Numerous DEP device for separation of CTCs have been reported in the literature but few have been able to obtain such a throughput. Shim et al. [53] successfully isolated CTCs using DEP Flow Field Fractionation at a rate of 0.25 mL/min. Gascoyne et. al. [54] processed sample at a rate of 0.3-0.6 mL/h using a DEP channel. Faraghat et. al. [16] achieved a flow rate of ~0.15 mL/h in each individual path in a DEP batch processing device containing 397 parallel paths, obtaining a combined flow rate of ~1 mL/min. In a hybrid DEP-DLD device Aghilinejad et. al. [27] achieved a flow rate of 0.002mL/min. Moon et al. [25] also developed a hybrid microfluidic device that combined DEP with multi-orifice flow fractionation and attained a flow rate of 0.126 mL/min. In the DEP inertial microfluidic device Khan and Chen [33] and Zhang et. al. [30] achieved a sample processing rate of 0.1 mL/min and 0.3 mL/min respectively in serpentine channels. The large separation distance

obtained in the spiral microchannel at high flow rate scenarios makes the device ideal for high throughput separation of overlapping sized cells.

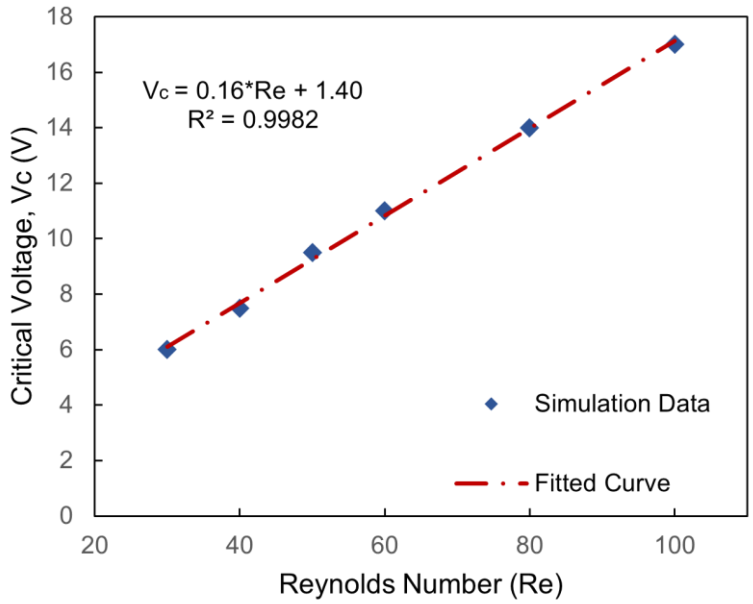

Figure 4.10 *Maximum lateral separation distance can be obtained at the critical voltage for the separation at different Reynolds numbers. Both the separation distance that can be achieved and the voltage at which maximum separation of the stream between CTC and WBC occurs increases with the increase in Reynolds number.*

4.5 Effects of the number of electrodes

Electric field strength plays a significant role in determining the focusing positions of the cells. In addition to the applied voltage of the external field, the number and placement of electrodes also determines the strength of the electrical field. To investigate the effect of the number of electrodes on separation, 60, 166, 190, 264, and 416 electrodes were placed up to the different sections of the channel. The lateral separation distance achieved at Re = 40 and 7.5V for a different number of electrodes is shown in Figure 4.11-a. It can be seen from the figure that as the number of electrodes is increased, the effective separation distance between WBCs and the

CTCs is increased. For 60 electrodes, the lateral separation distance between the particle is lowest, and from the trajectory of the cells in Figure 4.11-b it can be seen that both WBCs and the CTCs share a similar trajectory, and they can not be separated at different outlets. These cells travel from the outer wall of the spiral microchannel to the inner wall by the action of the dean force in the absence of any significant DEP force. For 166 electrodes, better separation is achieved as the effective length over which the cells experience the nDEP force increases. The state of the outlets when 60 and 416 electrodes are placed is shown in Figure 4.11-b and c, showing an increase in the lateral separation distance between CTCs and the WBCs when the number of electrodes is increased. It can be seen from the Figure 4.11-d and e that althogh the avergare magnitude of the DEP force experienced by the cells remains same in both the scenerio but the time and consequently the length over which the the cells experiecnce this DEP force increases as larger number of electrodes are used. Thus better separation could be observed when larger number of electrodes are used.

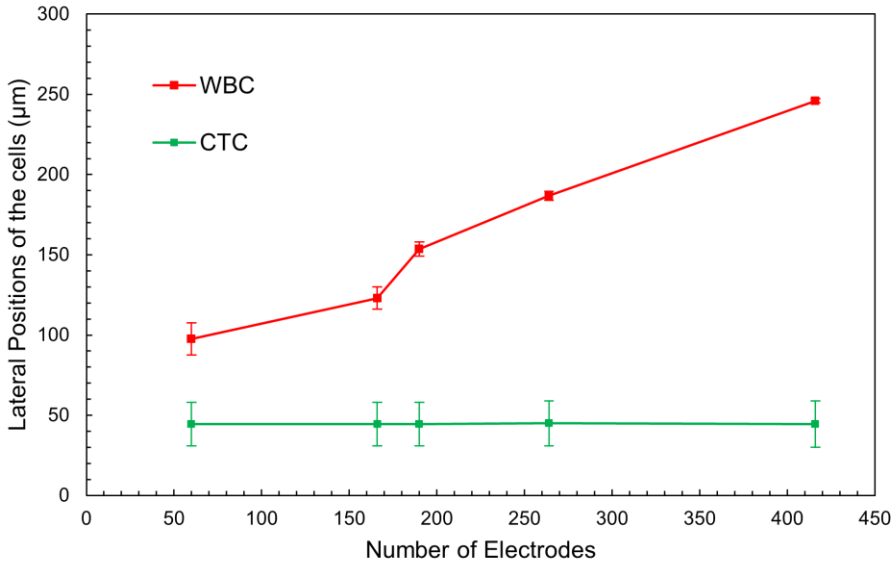

(a)

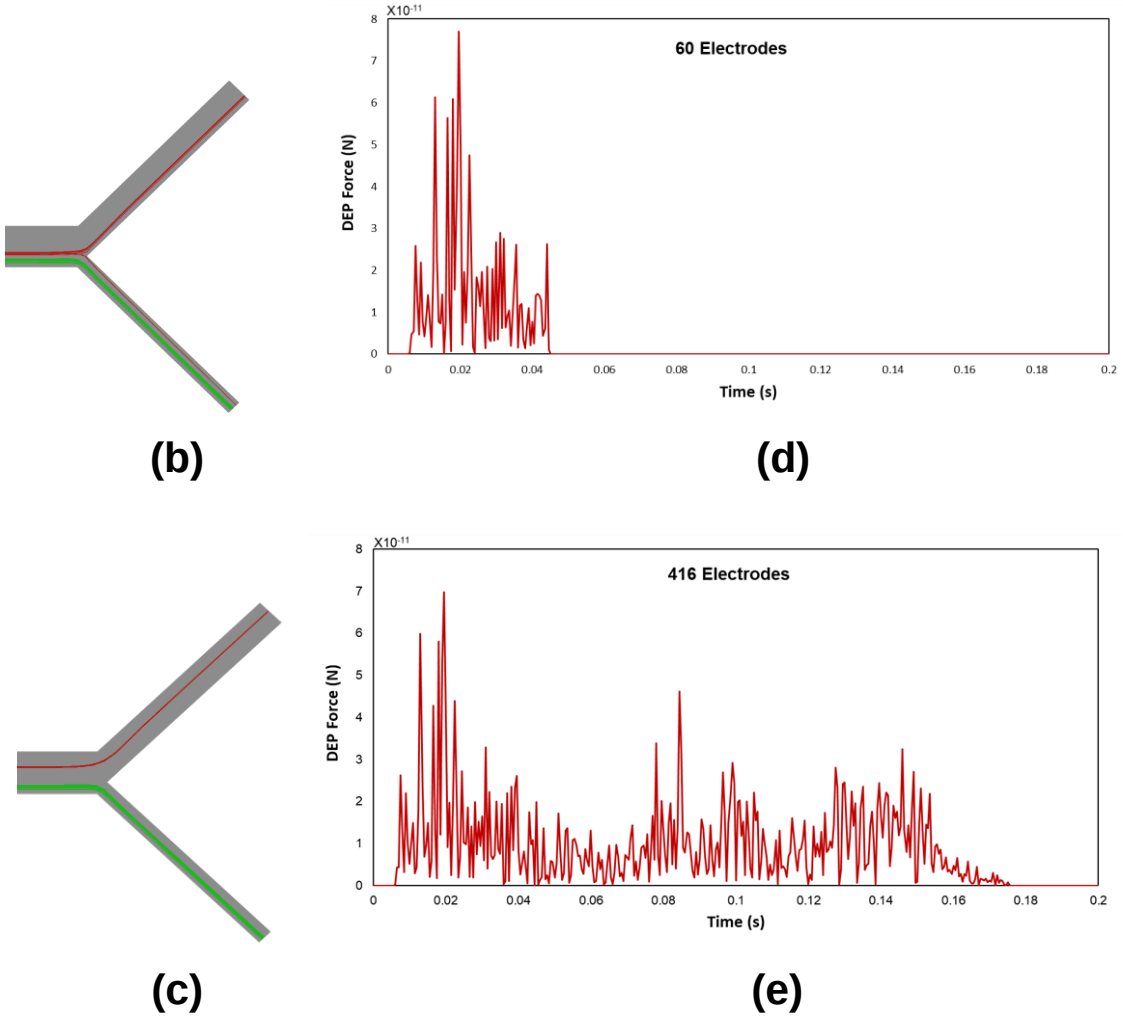

Figure 4.11 *Variation in the lateral separation distance of the cells achieved for the different number of electrodes placed at the bottom of the spiral channel. It can be seen that as the number of electrode increases the separation distance increases. (b) No apparent separation can be observed with 60 electrodes and (c) a lateral separation distance of 202 µm can be achived with 416 electrodes. From the DEP force experienced by the cells shown in figures (d) and (e)it can be seen that although both cells in both the configuration experience similar magnitude of DEP force but cells in 416 electrodes experience DEP force for more time and hence grater length of the channel.*

In addition to the number of electrodes, the placement of electrodes also influences the separation distance. It can be seen from Figure 4.12 larger separation distance can be achieved if the electrodes are placed from the inlet towards the start of the microchannel compared to the same number of electrodes if they are placed towards the end of the channel. Average separation distance

increases by almost 75 percent if the electrodes are placed toward the inlet. Additionally, the channel is devided into 5 sections (A-E) at start of the channel, 90°, 180° and towards at the end as shown in Figure 4.13-a-e and equal number of electrdoes is placed in those section. Placing 100 electrodes at those sections showed that the most effective separation of the particles occurs when the electrodes are placed towards the inlet of the channel as shown in Figure 4.13-f.

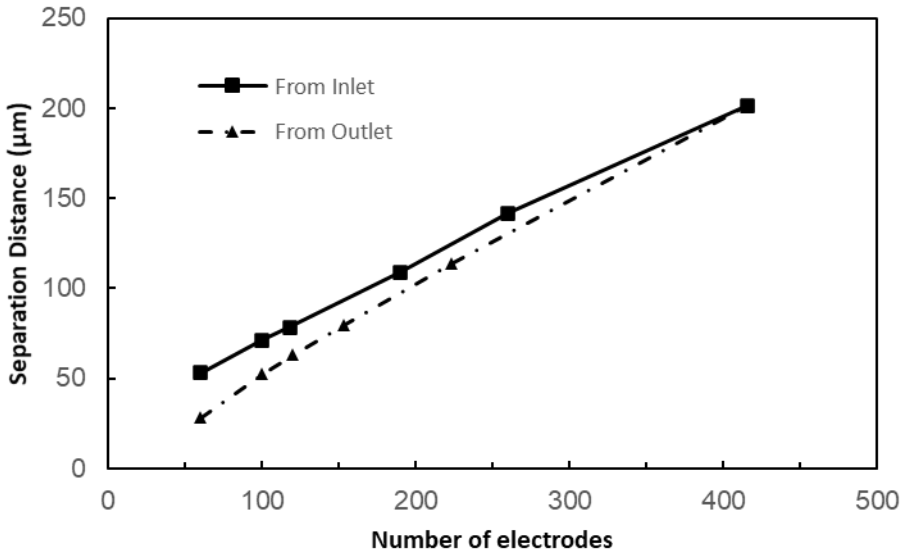

Figure 4.12 *The number and placement of the electrodes determines the separation distance. Better separation can be achived with more electrodes and if the electrodes are placed towards the inlet of the channel.*

Some vital observation from this parametric study is that both the WBCs and the CTCs do not change their focusing position down the length of the channel where no electrodes are placed, and placing the electrodes towards the start of the channel results in the most effective separation of the particles. These might prove crucial in the fabrication of microchannels for the separation of the cells. An average separation distance of 72 µm was achived when electrodes are placed in towards the beginning of the channel in section A which provides on averge 40% better separation compared to placement of electrodes at the other section of the channel.

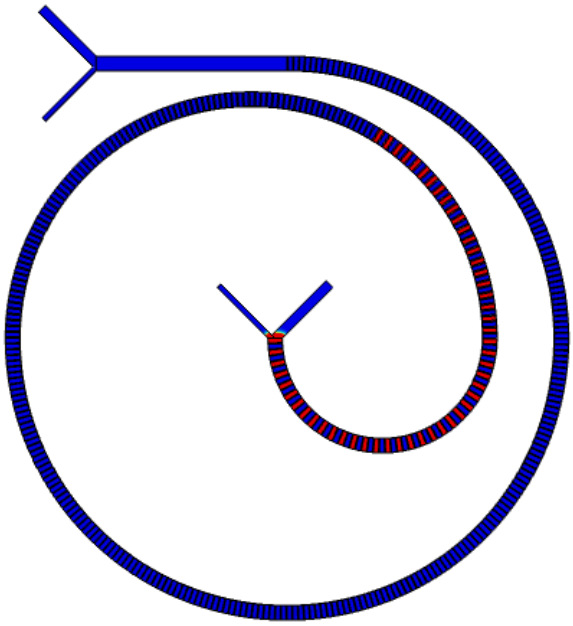

(a) Section A

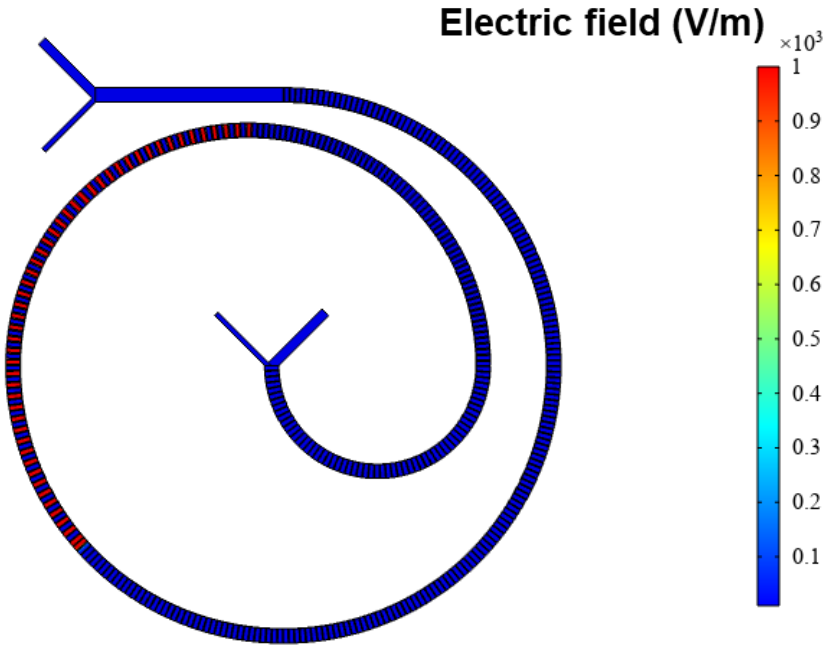

(b) Section B

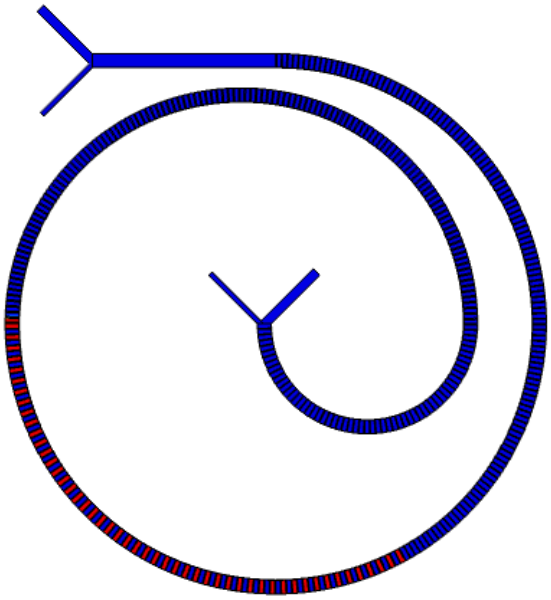

(c) Section C

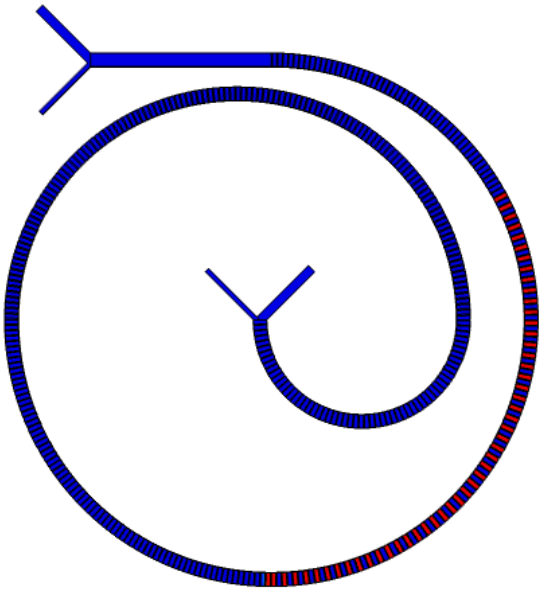

(d) Section D

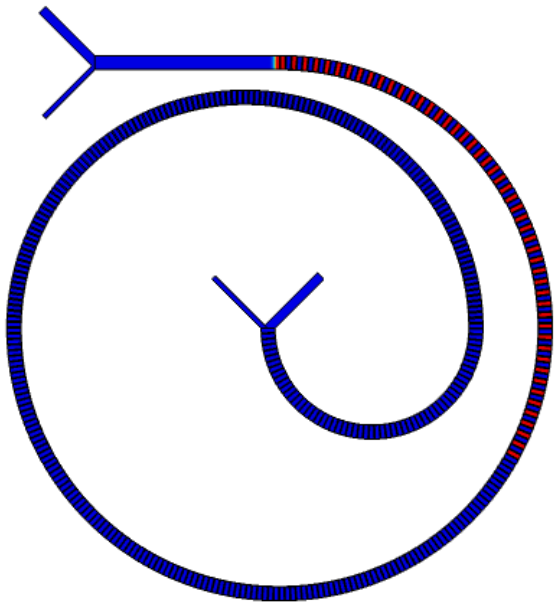

(e)Section E

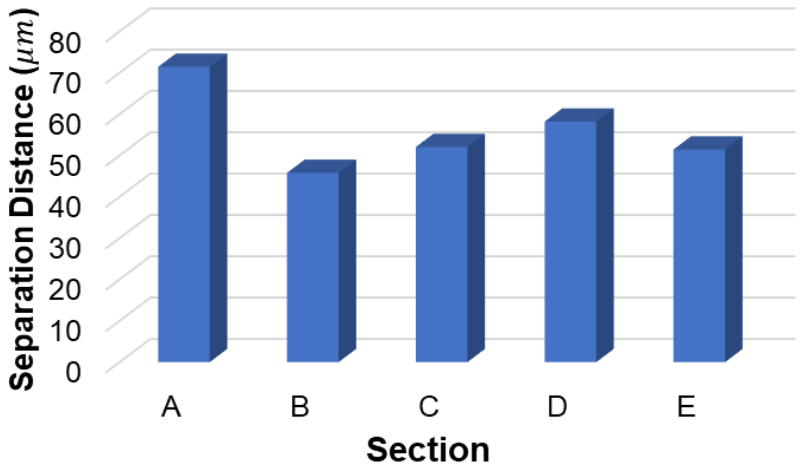

(f)

Figure 4.13 *100 electrodes are placed at five different sections (A-E) of the spiral microchannel to findout a region that provides most effective separation for a limited number of electrodes as shown in (a-e). The electric field strength generated by those electrode is illustrated in the figure. It can be seen from (f) that highest separation distance can be achieved if the electrodes are placed in section A, nearest to the inlet. For the other four sections the separation distance is almost similar.*

4.6 Effectiveness of the channel to separate CTCs from a mixture of WBCs

To demonstrate the robustness of the hybrid inertial dielectrophoretic spiral microchannel to separate CTCs from a mixture of different subtypes of WBCs, all the different subtypes of white blood cells were injected into the channel in addition to the same-sized larger WBCs and CTCs, and the separation effectiveness was investigated. The trajectories of the cells were captured in the absence and presence of an applied electric field. In the absence of an electric field, no separation between different cell types was observed, and all of the particles were found near the inner outlet of the channel as shown in Figure 4.14-a.

In the presence of the electric field CTCs, and all the different subtypes WBCs experience zero DEP and negative DEP force, respectively. In other words, in the such working region, CTCs are unaffected by the nonuniform electric field and still follow their initial trajectory towards the bottom of the channel. When an electric field is applied at the critical voltage of the large WBCs found in the earlier sets of simulations, it was observed, similar to the characteristics discussed previously, Granulocytes and Monocytes, each occupy two focusing positions at the top and bottom of the outlet as shown in Figure 4.14-b. On the other hand, the T-lymphocytes and the B-lymphocytes are found near the bottom of the channel. However, all four subtypes of WBCs demonstrated sufficient lateral displacement to be successfully separated from the CTCs at this voltage. This can be explained by the relative magnitude of the DEP force experienced by all the different WBCs. As shown in Figure 4.15 the average relative magnitude of the DEP force experienced by Granulocytes is similar to the DEP force experienced Monocytes. In contrast, the magnitude of the DEP force experienced by the T-Lymphocytes and B-Lymphocytes is much lower. Despite the relatively lower magnitude of the DEP force experienced by the Lymphocytes,

can still be separated by the inertial migration of the smaller cells in the presence of dean force in a curved spiral microchannel. Similar characteristics of the particles were observed in [27]. It can be deduced from such behavior of T-lymphocytes and B-lymphocytes that they will have a higher critical voltage of separation than granulocytes or monocytes. Still, their smaller size makes their separation by inertial microfluidics in the spiral channel possible.

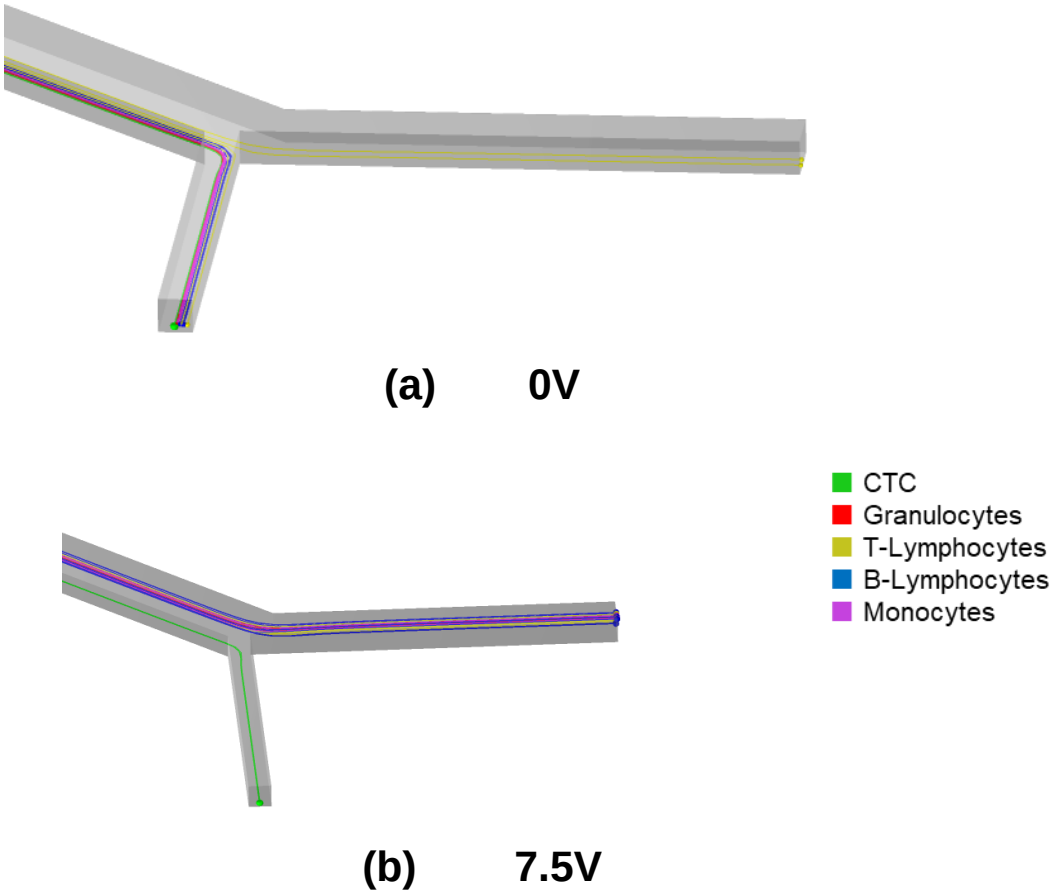

(a) 0V

(b) 7.5V

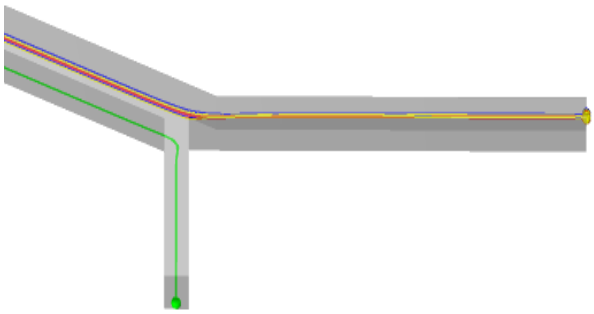

(c) 15V

Figure 4.14 *The spiral microchannel is able to separate CTCs from a mixture of WBCs with various sizes and dielectric properties in the presence of an electric field. (a) In the absence of any electric field all the cells follow the same trajectory (b) at the cirtical voltga of Granulocytes the other types of WBCs are also laterally separated and can be collected in a different outlet. (c) At voltage greater than the critical voltage all the different subtypes of WBCs occupy the top focusing position and also can be separated laterally.*

At voltages higher than the critical voltage, it was seen from Figure 4.14-b that all the WBCs now migrate to the top focusing position at the outlet. Additionally, it can also be observed that the lateral separation distance between the WBCs and the CTCs decreases, confirming results found in the previous simulations.

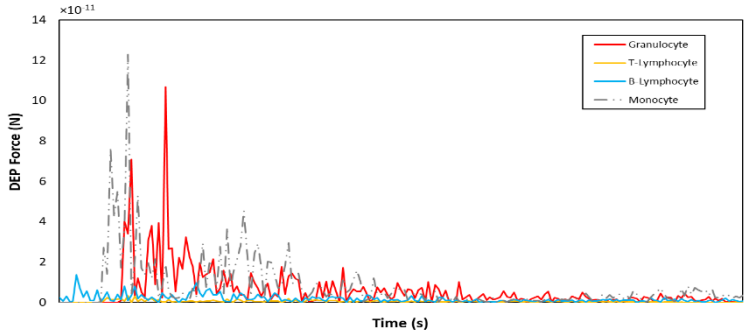

Figure 4.15 *The DEP force experienced by various sub types of WBC is shown in the figure. It can be seen that the magnitude of the DEP force experienced by the large WBCs, Granulocytes and Monocytes are similar in magnitude whereas the T-Lymphocytes and B-Lymphocytes experience much lower DEP force.*

CHAPTER 5: CONCLUSION

The focus of the current research is to develop a numerical model for a hybrid cell separation platform, with the objective of efficiently separating overlapping-sized CTCs from WBCs. The research also seeks to examine the migration behavior of cells in DEP electrode embedded spiral microchannel, as well as to elucidate the physics of flow inside these channels. While experimental work may yield more precise outcomes, it entails complicated research facilities and substantial expenses. Furthermore, experimental studies face challenges in visualizing the mechanisms of cell separation, induced forces, and cell trajectories. In contrast, numerical simulation offers a solution to these challenges by allowing for visualization of cell migration, trajectories, and induced forces in a time and cost-efficient manner. For these reason, in this study numerical modeling is used for numerical analysis of such cell separation mechanism.

In an electrode embedded curved microchannel a cell is acted upon by inertial lift force, dean drag force and the DEP force. The underlying theories and the corresponding equations behind these forces were discussed in details in the second chapter of this thesis. In the next chapter, the description of the numerical model that was developed to analyse the separation of WBCs from CTCs was described. A spiral microchannel with embedded electrodes is used to achieve high throughput separation of overlapping-sized cell CTCs from WBCs. There are four main subtypes of WBCs- Granulocytes, T-Lymphocytes, B-Lymphocytes, Monocytes. Due to the dielectric properties inherent to the WBCs, all the different subtypes of WBCs have cross-over frequency lower than the cross-over frequency of the CTCs. This differene in the dielectric properties of the cells was exploited to separate the CTCs from the the WBCs. To show the effectiveness of the channel to separate the overlapping sized cells Granulocytes were considered

as WBCs in the subsequent simulations as it this larger cell types have size similar to the size of the CTCs. By setting the frequency of the AC electric field to the crossover frequency of the CTCs, the DEP force selectively affects only the WBCs, causing them to migrate to the different part of channel where they can be effectively separated.

In the result section, the characteristics of the underlying forces are analyzed at different voltages and Reynolds numbers to shed lights on the separation mechanism. Firstly, the effect of the sheath flow on the trajectory of the cells was investigated. It was found that, for a sheath inlet less than 50 μm, all the cells occupy two vertical focusing position and no separation could be observed. A sheath inlet of 50 μm or greater is essential for pushing all the cell types to the bottom of the channel. Towards the bottom of the channel, only WBCs experience a substantial DEP force which pushes them upwards whereas the CTCs maintain their trajectory at the bottom of the channel. And the cells could essentially be separated. For a sheath inlet of 75 μm, both vertical and lateral separation of the cells were observed and this configuration was used for the subsequent analysis. In the next section, it has been shown in detail that, with the increase in the intensity of the electric field the focusing position of the CTCs remain unchanged. It has been found that at a voltage termed as critical voltage the WBCs occupy two vertical focusing position- at the top and the bottom of the channel. The particles are also laterally displaced as a voltage is applied and maximum lateral separation is obtained at the critical voltage. The inertial-DEP hybrid device is demonstrated to successfully separate overlapping sized CTCs from WBCs and it is shown to provide a high lateral separation distance of 120 μm with 190 electrodes at a low applied peak-to-peak voltage of 7.5V at a Reynolds number of 40. The vertical and lateral migration of the cells were explain in light of the inertial forces, dean drag force and the DEP force in the third result section. In the next result section, the effect of the the throughout on the separation effectiveness

was investigated. It has been shown that with the increase in the Reynolds number the critical voltage as well as the separation distance between the cells increases. However, the increase in the separation distance saturates at higher Reynolds number. The effect of the number of electrodes on the separation distance was investiagated and it was found that the separation distance between the CTCs and the WBCs increases with the increase in the Reynolds number. And a larger separation distance could be obtained if the electrodes were placed towards the inlet compared to positioning the electrodes towards the outlet. Finally, the robustness of the system to isolate CTCs from a mixture of different types of WBCs was investigated. It was found that, although Granulocytes and Monocytes experienced higher DEP force and had a lower critical voltage than the lymphocytes, but the smaller sizes of the lymphocytes made them more susceptible to the inertial and dean vortices which resulted in the lateral migration of all the different WBCs to the outer outlet whereas CTCs can be collected through the inner outlet. Due to the enourmous time required to simulate and study the separation characteristics of all the different sub types of WBCs, only the Granulocytes were considered for the other studies previously mentioned and it was shown that the behaviour of the WBCs and CTCs were similar in both the scenario.

The proposed device provides a mechanism for high throughput separation of the overlapping sized cell particles by leveraging the benefits of both DEP and inertial microfluidic techniques. Additionally, the device was also shown to be effective for separation of CTCs from mixture of WBCs. Moreover, such a microfluidic platform can be utilized to effectively manipulate and separate any cell population by simply adjusting the electric field without requiring any specific device design for each different cell mixture. For future studies, the properties of buffer solutions can be adjusted to imitate the real cell medium utilized in clinical settings. Additionally, the conductivity of the cell medium can be modified to achieve separation with a lower electric

field intensity. Finally, it is worth considering other electrode configuration in addition to the radial electrodes for the cell separation.

REFERNCES

[1] G. T. Budd *et al.*, “CirculatingTumor Cells versus ImagingöPredicting Overall Survival in Metastatic Breast Cancer”, doi: 10.1158/1078-0432.CCR-05-1769.

[2] P. Bankó *et al.*, “Technologies for circulating tumor cell separation from whole blood,” *Journal of Hematology and Oncology*, vol. 12, no. 1. BioMed Central Ltd., May 14, 2019. doi: 10.1186/s13045-019-0735-4.

[3] C. Yang, B. R. Xia, W. L. Jin, and G. Lou, “Circulating tumor cells in precision oncology: Clinical applications in liquid biopsy and 3D organoid model,” *Cancer Cell International*, vol. 19, no. 1. BioMed Central Ltd., Dec. 18, 2019. doi: 10.1186/s12935-019-1067-8.

[4] W. J. Allard *et al.*, “Tumor Cells Circulate in the Peripheral Blood of All Major Carcinomas but not in Healthy Subjects or Patients With Nonmalignant Diseases,” *Clinical Cancer Research*, vol. 10, no. 20, pp. 6897–6904, Oct. 2004, doi: 10.1158/1078-0432.CCR-04-0378.

[5] L. Wang, P. Balasubramanian, A. P. Chen, S. Kummar, Y. A. Evrard, and R. J. Kinders, “Promise and limits of the CellSearch platform for evaluating pharmacodynamics in circulating tumor cells,” *Seminars in Oncology*, vol. 43, no. 4, pp. 464–475, Aug. 2016, doi: 10.1053/J.SEMINONCOL.2016.06.004.

[6] C. Wyatt Shields Iv, C. D. Reyes, and G. P. López, “Microfluidic cell sorting: A review of the advances in the separation of cells from debulking to rare cell isolation,” *Lab on a Chip*, vol. 15, no. 5. Royal Society of Chemistry, pp. 1230–1249, Mar. 07, 2015. doi: 10.1039/c4lc01246a.

[7] M. T. Gabriel, L. R. Calleja, A. Chalopin, B. Ory, and D. Heymann, “Circulating tumor cells: A review of Non-EpCAM-based approaches for cell enrichment and isolation,” *Clinical Chemistry*, vol. 62, no. 4. American Association for Clinical Chemistry Inc., pp. 571–581, Apr. 01, 2016. doi: 10.1373/clinchem.2015.249706.

[8] K. Jacob, C. Sollier, and N. Jabado, “Circulating tumor cells: Detection, molecular profiling and future prospects,” *Expert Review of Proteomics*, vol. 4, no. 6. 2007. doi: 10.1586/14789450.4.6.741.

[9] M. A. Hashem, A. Aghilinejad, X. Chen, and H. Tan, “Compound Droplet Modeling for Circulating Tumor Cell Microfiltration With Adaptive Meshing Refinement,” 2020, doi: 10.1115/1.4048134.

[10] T. Salafi, K. K. Zeming, and Y. Zhang, “Advancements in microfluidics for nanoparticle separation,” *Lab on a Chip*, vol. 17, no. 1, pp. 11–33, Jan. 2017, doi: 10.1039/C6LC01045H.

[11] A. Dalili, E. Samiei, and M. Hoorfar, “A review of sorting, separation and isolation of cells and microbeads for biomedical applications: microfluidic approaches,” *Analyst*, vol. 144, no. 1, pp. 87–113, 2019, doi: 10.1039/c8an01061g.

[12] M. Hejazian and N. T. Nguyen, “Negative magnetophoresis in diluted ferrofluid flow,” *Lab on a Chip*, vol. 15, no. 14, pp. 2998–3005, Jun. 2015, doi: 10.1039/C5LC00427F.

[13] M. Ward, P. Turner, M. DeJohn, and G. Kaduchak, “Fundamentals of Acoustic Cytometry,” *Current Protocols in Cytometry*, vol. 49, no. 1, p. 1.22.1-1.22.12, Jul. 2009, doi: 10.1002/0471142956.CY0122S49.

[14] O. D. Velev, S. Gangwal, and D. N. Petsev, “Particle-localized AC and DC manipulation and electrokinetics,” *Annual Reports Section “C” (Physical Chemistry)*, vol. 105, no. 0, pp. 213–246, Apr. 2009, doi: 10.1039/B803015B.

[15] J. Voldman, “ELECTRICAL FORCES FOR MICROSCALE CELL MANIPULATION,” *http://dx.doi.org/10.1146/annurev.bioeng.8.061505.095739*, vol. 8, pp. 425–454, Jul. 2006, doi: 10.1146/ANNUREV.BIOENG.8.061505.095739.

[16] S. A. Faraghat *et al.*, “High-throughput, low-loss, low-cost, and label-free cell separation using electrophysiology-activated cell enrichment,” *Proceedings of the National Academy of Sciences of the United States of America*, vol. 114, no. 18, pp. 4591–4596, May 2017, doi: 10.1073/PNAS.1700773114.

[17] F. S. Iliescu *et al.*, “Highlighting the uniqueness in dielectrophoretic enrichment of circulating tumor cells,” *ELECTROPHORESIS*, vol. 40, no. 10, pp. 1457–1477, May 2019, doi: 10.1002/ELPS.201800446.

[18] G. Stemme and G. Kittilsland, “New fluid filter structure in silicon fabricated using a self-aligning technique,” *Applied Physics Letters*, vol. 53, no. 16, p. 1566, Nov. 1998, doi: 10.1063/1.99953.

[19] D. D. Carlo, “Inertial microfluidics,” *Lab on a Chip*, vol. 9, no. 21, pp. 3038–3046, 2009, doi: 10.1039/b912547g.

[20] L. R. Huang, E. C. Cox, R. H. Austin, and J. C. Sturm, “Continuous Particle Separation Through Deterministic Lateral Displacement,” *Science*, vol. 304, no. 5673, pp. 987–990, May 2004, doi: 10.1126/SCIENCE.1094567/SUPPL_FILE/HUANG.SOM.PDF.

[21] M. Yamada, M. Nakashima, and M. Seki, “Pinched flow fractionation: Continuous size separation of particles utilizing a laminar flow profile in a pinched microchannel,” *Analytical Chemistry*, vol. 76, no. 18, pp. 5465–5471, Sep. 2004, doi: 10.1021/AC049863R/SUPPL_FILE/AC049863RSI20040123_054437.AVI.

[22] E. Gioe, M. R. Uddin, J. H. Kim, and X. Chen, “Deterministic Lateral Displacement (DLD) Analysis Tool Utilizing Machine Learning towards High-Throughput Separation,”

Micromachines 2022, Vol. 13, Page 661, vol. 13, no. 5, p. 661, Apr. 2022, doi: 10.3390/MI13050661.

[23] B. M. Dincau, A. Aghilinejad, X. Chen, S. Y. Moon, and J. H. Kim, "Vortex-free high-Reynolds deterministic lateral displacement (DLD) via airfoil pillars," *Microfluidics and Nanofluidics*, vol. 22, no. 12, Dec. 2018, doi: 10.1007/s10404-018-2160-3.

[24] J. P. Beech, P. Jönsson, and J. O. Tegenfeldt, "Tipping the balance of deterministic lateral displacement devices using dielectrophoresisY," *Lab on a Chip*, vol. 9, no. 18, pp. 2698–2706, 2009, doi: 10.1039/b823275j.

[25] H. S. Moon *et al.*, "Continuous separation of breast cancer cells from blood samples using multi-orifice flow fractionation (MOFF) and dielectrophoresis (DEP)," *Lab on a Chip*, vol. 11, no. 6, pp. 1118–1125, Feb. 2011, doi: 10.1039/C0LC00345J.

[26] M. Rahmati and X. Chen, "Separation of circulating tumor cells from blood using dielectrophoretic DLD manipulation," *Biomedical Microdevices*, vol. 23, no. 4, Dec. 2021, doi: 10.1007/s10544-021-00587-8.

[27] M. Aghaamoo, A. Aghilinejad, X. Chen, and J. Xu, "On the design of deterministic dielectrophoresis for continuous separation of circulating tumor cells from peripheral blood cells," *Electrophoresis*, vol. 40, no. 10, pp. 1486–1493, May 2019, doi: 10.1002/elps.201800459.

[28] C. Church, J. Zhu, and X. Xuan, "Negative dielectrophoresis-based particle separation by size in a serpentine microchannel," *Electrophoresis*, vol. 32, no. 5, pp. 527–531, Feb. 2011, doi: 10.1002/elps.201000396.

[29] J. Zhu, R. C. Canter, G. Keten, P. Vedantam, T. R. J. Tzeng, and X. Xuan, "Continuous-flow particle and cell separations in a serpentine microchannel via curvature-induced dielectrophoresis," *Microfluidics and Nanofluidics*, vol. 11, no. 6, pp. 743–752, Dec. 2011, doi: 10.1007/s10404-011-0839-9.

[30] J. Zhang *et al.*, "Tunable particle separation in a hybrid dielectrophoresis (DEP)- inertial microfluidic device," *Sensors and Actuators, B: Chemical*, vol. 267, pp. 14–25, Aug. 2018, doi: 10.1016/j.snb.2018.04.020.

[31] D. Marrinucci *et al.*, "Cytomorphology of Circulating Colorectal Tumor Cells: A Small Case Series," *Journal of Oncology*, vol. 2010, pp. 1–7, 2010, doi: 10.1155/2010/861341.

[32] C. Jin *et al.*, "Technologies for label-free separation of circulating tumor cells: From historical foundations to recent developments," *Lab on a Chip*, vol. 14, no. 1. Royal Society of Chemistry, pp. 32–44, Jan. 07, 2014. doi: 10.1039/c3lc50625h.

[33] M. Khan and X. Chen, “Numerical study of dielectrophoresis-modified inertial migration for overlapping sized cell separation,” *ELECTROPHORESIS*, vol. 43, no. 7–8, pp. 879–891, Apr. 2022, doi: 10.1002/ELPS.202100187.

[34] M. S. Islam, M. R. Uddin, and X. Chen, “Circulating Tumor Cell Separation in a Zigzag Channel Using Dielectrophoresis Based Inertial Microfluidics,” presented at the ASME 2022 International Mechanical Engineering Congress and Exposition, American Society of Mechanical Engineers Digital Collection, Feb. 2023. doi: 10.1115/IMECE2022-95384.

[35] P. R. C. Gascoyne and S. Shim, “Isolation of Circulating Tumor Cells by Dielectrophoresis,” *Cancers*, vol. 6, no. 1, p. 545, 2014, doi: 10.3390/CANCERS6010545.

[36] H. Amini, W. Lee, and D. Di Carlo, “Inertial microfluidic physics,” *Lab Chip*, vol. 14, no. 15, p. 2739, 2014, doi: 10.1039/c4lc00128a.

[37] G. Segré and A. Silberberg, “Radial Particle Displacements in Poiseuille Flow of Suspensions,” *Nature 1961 189:4760*, vol. 189, no. 4760, pp. 209–210, 1961, doi: 10.1038/189209a0.

[38] S. Ookawara, D. Street, and K. Ogawa, “Numerical study on development of particle concentration profiles in a curved microchannel,” *Chemical Engineering Science*, vol. 61, no. 11, pp. 3714–3724, 2006, doi: 10.1016/j.ces.2006.01.016.

[39] A. A. S. Bhagat, S. S. Kuntaegowdanahalli, and I. Papautsky, “Continuous particle separation in spiral microchannels using dean flows and differential migration,” *Lab on a Chip*, vol. 8, no. 11, pp. 1906–1914, 2008, doi: 10.1039/b807107a.

[40] H. A. Nieuwstadt *et al.*, “Microfluidic particle sorting utilizing inertial lift force,” *Biomedical Microdevices 2010 13:1*, vol. 13, no. 1, pp. 97–105, Sep. 2010, doi: 10.1007/S10544-010-9474-6.

[41] G. De Gasperis, J. Yang, F. F. Becker, P. R. C. Gascoyne, and X.-B. Wang, “Micro¯uidic Cell Separation by 2-dimensional Dielectrophoresis,” 1999.

[42] D. Kim, M. Sonker, and A. Ros, “Dielectrophoresis: From Molecular to Micrometer-Scale Analytes,” *Analytical Chemistry*, vol. 91, no. 1, pp. 277–295, Jan. 2019, doi: 10.1021/ACS.ANALCHEM.8B05454/ASSET/IMAGES/LARGE/AC-2018-05454H_0005.JPEG.

[43] H. W. Hou *et al.*, “Isolation and retrieval of circulating tumor cells using centrifugal forces,” *Scientific Reports*, vol. 3, 2013, doi: 10.1038/srep01259.

[44] J. Cottet, O. Fabregue, C. Berger, F. Buret, P. Renaud, and M. Frénéa-Robin, “MyDEP: A New Computational Tool for Dielectric Modeling of Particles and Cells,” *Biophysical Journal*, vol. 116, no. 1, pp. 12–18, Jan. 2019, doi: 10.1016/j.bpj.2018.11.021.

[45] P. R. C. Gascoyne, S. Shim, J. Noshari, F. F. Becker, and K. Stemke-Hale, "Correlations between the dielectric properties and exterior morphology of cells revealed by dielectrophoretic field-flow fractionation," *Electrophoresis*, vol. 34, no. 7, pp. 1042–1050, Apr. 2013, doi: 10.1002/ELPS.201200496.

[46] J. Prinyakupt and C. Pluempitiwiriyawej, "Segmentation of white blood cells and comparison of cell morphology by linear and naïve Bayes classifiers," *BioMedical Engineering Online*, vol. 14, no. 1, pp. 1–19, Jun. 2015, doi: 10.1186/S12938-015-0037-1/TABLES/8.

[47] S. I. Han, Y. D. Joo, and K. H. Han, "An electrorotation technique for measuring the dielectric properties of cells with simultaneous use of negative quadrupolar dielectrophoresis and electrorotation," *Analyst*, vol. 138, no. 5, pp. 1529–1537, Mar. 2013, doi: 10.1039/c3an36261b.

[48] E. Klaseboer, J. P. Chevaillier, A. Mate, O. Masbernat, and C. Gourdon, "Model and experiments of a drop impinging on an immersed wall," *Physics of Fluids*, vol. 13, no. 1, p. 45, Dec. 2000, doi: 10.1063/1.1331313.

[49] Fuat Yilmaz and Mehmet Yasar Gundogdu, "Analysis of conventional drag and lift models for multiphase CFD modeling of blood flow," *Korea-Australia Rheology Journal*, vol. 21, no. 3, pp. 161–173, 2009.

[50] P. J. Roache, "QUANTIFICATION OF UNCERTAINTY IN COMPUTATIONAL FLUID DYNAMICS," *Annu. Rev. Fluid. Mech*, vol. 29, pp. 123–60, 1997.

[51] J. Zhang, S. Yan, G. Alici, N. T. Nguyen, D. Di Carlo, and W. Li, "Real-time control of inertial focusing in microfluidics using dielectrophoresis (DEP)," *RSC Advances*, vol. 4, no. 107, pp. 62076–62085, 2014, doi: 10.1039/c4ra13075h.

[52] D. Di Carlo, "Inertial microfluidics," *Lab on a Chip*, vol. 9, no. 21. Royal Society of Chemistry, pp. 3038–3046, 2009. doi: 10.1039/b912547g.

[53] S. Shim, K. Stemke-Hale, A. M. Tsimberidou, J. Noshari, T. E. Anderson, and P. R. C. Gascoyne, "Antibody-independent isolation of circulating tumor cells by continuous-flow dielectrophoresis," *Biomicrofluidics*, vol. 7, no. 1, Feb. 2013, doi: 10.1063/1.4774304.

[54] Y. Huang, X. B. Wang, F. F. Becker, and P. R. C. Gascoyne, "Introducing dielectrophoresis as a new force field for field-flow fractionation," *Biophysical Journal*, vol. 73, no. 2, pp. 1118–1129, Aug. 1997, doi: 10.1016/S0006-3495(97)78144-X.